Ocean Engineering 186 (2019) 106055

Contents lists available at ScienceDirect

Ocean Engineering

journal homepage: www.elsevier.com/locate/oceaneng

Statistical modelling of extreme ocean current velocity profiles

Pål T. Bore [a,*], Jørgen Amdahl [a], David Kristiansen [b]

[a] Department of Marine Technology, Norwegian University of Science and Technology (NTNU), Otto Nielsens Veg 10, 7491 Trondheim, Norway
[b] SINTEF Ocean, Brattørkaia 17C, 7465 Trondheim, Norway

ARTICLE INFO

Keywords:
Current velocity profiles
Extreme current velocities
Multivariate extreme values
Conditional extremes model
Peaks over threshold
Structural design

ABSTRACT

Knowledge about extreme ocean currents and their vertical structure is important when designing offshore structures. We propose a method for statistical modelling of extreme vertical current velocity profiles, accounting for factors such as directionality, spatial and temporal dependence, and non-stationarity due to the tide. We first pre-process the data by resolving the observed (vector) currents at each of several water depths into orthogonal major and minor axis components by principal component analysis, and use harmonic analysis to decompose the total (observed) current into the sum of (deterministic) tidal and (stochastic) residual currents. A complete marginal model is then constructed for all residual current components, and the dependence structure between the components is characterized using the conditional extremes model by Heffernan and Tawn (2004). By simulating under this model, estimates of various extremal statistics can be acquired. A simple approach for deriving design current velocity profiles is also proposed. The method is tested using measured current profiles at two coastal locations in Norway, covering a period of 2.5 and 1.5 years. It is demonstrated that the method provides good extrapolations at both locations, and the estimated 10-year design current velocity profiles appear realistic compared to the most extreme velocity profiles observed in the measurements.

1. Introduction

Knowledge about ocean currents and their vertical structure is important as a design criterion for ocean and coastal structures. For offshore structures located in shallow water, waves are typically the most important load factor, while in deeper water, currents can actually dominate the load equation (Forristall and Cooper, 1997). This is also the case for many structures located in the coastal zone, where coastal features such as islands and skerries can provide shelter from severe sea states, whilst currents might retain, or even increase, their strength. An example of the latter type of structure is aquaculture fish cages, where the mooring line tension is generally dominated by current loads (Huang et al., 2008). It is clear that simplification of the vertical current profile can introduce substantial errors in the calculated design load in such cases. In a review paper on recent developments of ocean environmental description (Bitner-Gregersen et al., 2014), improved accuracy of the statistical description of currents is called for; particularly regarding change of the current profile with water depth. This issue is addressed in the present paper.

Unlike many other time signals in nature, ocean currents include a deterministic signal due to the astronomical tide, generally becoming much stronger and important near the shore and in shallow water (Pugh and Woodworth, 2014). Applying standard tidal analysis techniques, the tidal signal can be extracted and predicted with very high accuracy for 'any' future time (Robinson and Tawn, 1997). Currents have this in common with sea-levels, so the methods used for estimating the distribution of extreme currents and sea-levels are therefore somewhat related. Two broad classes of methods exist: (1) *Direct methods*, analysing extremes of the total (observed) current directly, and (2) *indirect methods*, exploiting the decomposition of the total current into (deterministic) tidal and (stochastic) residual currents, modelling both separately before inferring the distribution of extreme total currents. Our focus will be on the second class, sometimes referred to as the joint probabilities method (JPM). This method was originally introduced for estimation of extreme sea-levels by Pugh and Vassie (1978, 1980), and later applied for estimating extreme currents by Pugh (1982). Extensions were given by Robinson and Tawn (1997), demonstrating substantial benefits over traditional direct methods. For sea-levels, Dixon and Tawn (1999) found that the observed bias in direct methods was primarily caused by the non-stationarity introduced by the tide.

Extreme currents are far more difficult to estimate than extreme sea-levels, not only due to their directional and spatial variation, but also because of the difficulty of obtaining sufficiently long series of observations (Pugh and Woodworth, 2014). Even if a long time series

* Corresponding author.
E-mail addresses: paal.takle.bore@ntnu.no (P.T. Bore), jorgen.amdahl@ntnu.no (J. Amdahl), david.kristiansen@sintef.no (D. Kristiansen).

https://doi.org/10.1016/j.oceaneng.2019.05.037
Received 19 November 2018; Received in revised form 14 May 2019; Accepted 19 May 2019
Available online 13 June 2019

is available, a particular issue when dealing with extremes is that rare events are necessarily unusual, so the quantity of directly relevant observations is limited. This difficulty is compounded in the spatial setting (such as for current profiles) because forecasting then requires extrapolation into a high-dimensional space, with all its associated uncertainties. It is thus important that the statistical models used should both be flexible and have a strong mathematical foundation, so that such extrapolation has an adequate basis (Davison et al., 2012).

Arguably, the most useful and flexible current approach for modelling extremes in high dimensions is the conditional extremes model by Heffernan and Tawn (2004). Based on an assumption of the asymptotic form of the conditional distribution of a d-dimensional variable, given that it has an extreme component, they present a semiparametric approach valid for extremes from a wide class of multivariate distributions, applicable to problems of any dimension. Examples of application are spatial risk assessment of extreme river flows (Keef et al., 2009), joint modelling of extreme significant wave height and spectral peak period (Jonathan et al., 2010, 2013), modelling of temporal dependence in river flows (Eastoe and Tawn, 2012) and modelling spatial extremal dependence of sea surface elevations at neighbouring locations (Eastoe et al., 2013). The conditional extremes model was introduced for joint modelling of vertical current profiles by Jonathan et al. (2012), and Raghupathi et al. (2016) applied it both for joint modelling of currents and waves, and for modelling of current profiles. Owing to the positive experiences of the mentioned authors in using the Heffernan and Tawn model and its solid theoretical foundation, this model will be applied here as well. The additional constraints and slight change in model formulation recently proposed by Keef et al. (2013), are also implemented to overcome a few complications that have been identified with using the Heffernan and Tawn model.

As commented by Jonathan et al. (2012), any viable approach to modelling extreme vertical current velocity profiles must account for (a) the vector nature of the current at each depth, and (b) the dependence between currents at different depths. Instead of using empirical orthogonal functions (EOF) to pre-process the data and then perform extreme value analysis on just a few energetic modes of the observed current profiles (see, e.g., Forristall and Cooper (1997)), we choose to model orthogonal current components at each depth directly to avoid loss of information. Our approach is therefore closely related to that presented by Jonathan et al. (2012), however, we focus on modelling 'instantaneous' mean velocity profiles rather than profiles consisting of hourly maxima and minima of the current components. By considering orthogonal current components at each depth, we bypass the necessity of explicitly introducing covariates (as would be required for modelling current speeds and directions; see Raghupathi et al. (2016)).

The proposed method accommodates the vector nature of the current by considering orthogonal current components at each depth, and the dependence between the (residual) current components is characterized by the conditional extremes model. Furthermore, observed temporal dependence, leading to clustering of extremes, is accounted for in both the marginal tail and dependence modelling by applying the peaks over threshold (POT) method, and the non-stationarity introduced by tidal currents is handled by exploiting the decomposition of the total current into tidal and residual currents. The key steps of the proposed method are summarized in Fig. 1. We outline each of the steps herein, and also propose a simple and pragmatic approach for deriving design current velocity profiles. The method is believed to provide a valuable addition to existing methods for estimation of extreme current velocity profiles, and we test it using ADCP (acoustic Doppler current profiler) data collected at two coastal locations in Norway.

The paper is organized as follows. In Section 2, the considered locations, together with the available data, are described. A brief, general discussion on the accuracy of the measurements is also included. The required pre-processing of the data is described in Section 3. This includes application of principal component analysis (PCA) to resolve the current velocities into major and minor axis components

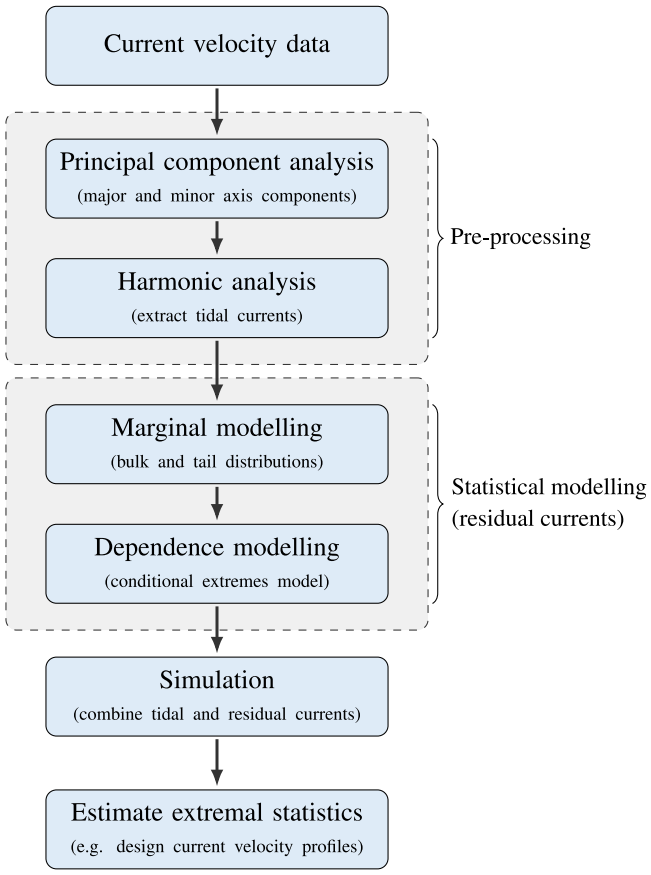

Fig. 1. Flowchart of the steps involved in the proposed method for estimation of design current velocity profiles.

at each depth and decomposition of the current velocity into tidal and residual currents by harmonic analysis. In Section 4, a general introduction of the conditional extremes model by Heffernan and Tawn (2004) is given. Section 5 constitutes the main part of this paper. Here, the statistical modelling of the residual current components is described in detail and applied to obtain extreme vertical residual and total current profiles at the two considered locations. We present an approach for modelling the complete marginal distribution (bulk and tail distribution) of each residual current component, describe the application of the conditional extremes model for characterizing the dependence structure between the components, and outline the Monte Carlo procedure used to simulate extreme residual current and total current velocity profiles. The simulated velocity profiles are compared with the measurements. In Section 6, a simple approach for deriving design current velocity profiles is proposed, and the main conclusions and a discussion on assumptions and possible improvements are given in Section 7.

2. Locations and data

As indicated in Fig. 2, the measurements have been made at two coastal locations off the west coast of Trndelag, Norway, roughly 150 km east of the shelf break. The *Munkskjæra* site (63.8221 N, 8.3836 E) has a water depth of approximately 80 m, and is located in vicinity of a number of small islands and skerries, forming a strait in the east–west direction. Fifteen kilometres to the northeast, at *Salatskjæra* (63.9200 N, 8.5927 E), the water depth is approximately 40 m. This site is surrounded by a myriad of small islands, underwater rocks and skerries, resulting in a local bathymetry that is even more complex than at Munkskjæra. A simple statistical analysis of the current and wave

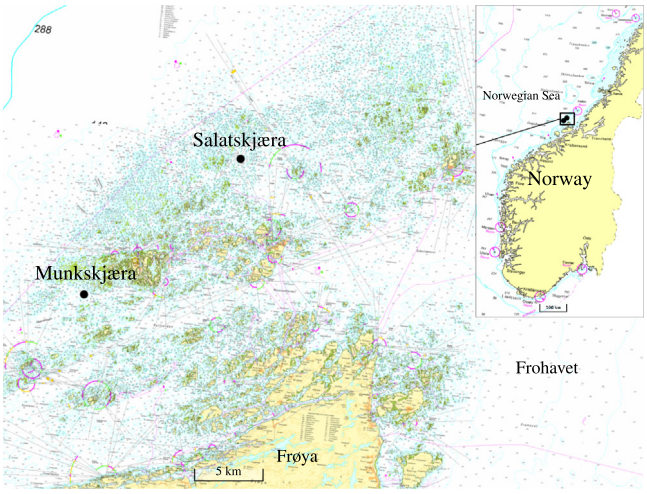

Fig. 2. Nautical chart showing the two considered locations (Source: The Norwegian Mapping Authority).

conditions at both sites has previously been made at an earlier stage of the measurement programme (Kristiansen et al., 2017).

There are two major current systems in this coastal area; the Norwegian Atlantic Current, primarily flowing along the shelf edge, and the Norwegian Coastal Current, causing high current speeds near the coast (Sætre, 2007). The larger fjord systems along the coastline are forced by freshwater runoff from land, resulting in a surface outflow of brackish water that eventually adds to the Norwegian Coastal Current (Broch et al., 2017). From the island Frya (see Fig. 2), a chain of small islands, stretches north-eastward. Between this island chain and the mainland of Norway, is a deep ocean bay, Frohavet, cutting inwards towards the entrance of Trondheimsfjorden. The local flow conditions at the considered sites (Munkskjæra and Salatskjæra) are dominated by water exchange between the Norwegian Sea (to the west) and Frohavet, primarily following the semidiurnal tidal cycle. Wind-induced currents are of importance too, and the rough topography creates a dynamic environment, including tidal residual currents generated by interaction of tidal currents with coastal features and bottom topography, and is also responsible for steering the current along its contours.

The measurements at both locations were made with a three-beam acoustic Doppler current profiler (ADCP) of type Nortek Aquadopp 400 kHz, mounted on a moored oceanographic surface buoy (Seawatch Midi 185). An ADCP utilizes a physical principle called the Doppler effect to measure the current speed and direction in multiple depth cells through the water column. The Doppler effect is exploited by emitting sound pulses from transducers (beams) which are reflected (echoed) by particulate matter moving with the water. The signal is then shifted in frequency (Doppler shifted) in proportion to the particle velocity; see, e.g., Nortek (2017) for additional information. Note that the resulting measured velocity vector (in a given depth cell) by an ADCP is not an instantaneous velocity at a fixed point, but rather a spatial average with an inherent assumption that the flow is homogeneous in the horizontal plane over the distances separating the acoustic beams (Lu and Lueck, 1999). The current measurements were performed with a sampling rate of 1 Hz over an ensemble interval of 10 min (600 samples) with output once every hour. This yields a time series of hourly (10 min average) current speeds and directions. The speed range was 0–300 cm/s, discretized by 256 points (bin size of 1.2 cm/s), and the depth cell size was 3 m. The data were post-processed internally on the buoy before being sent to land every hour.

The measurement period at Munkskjæra was almost 2.5 years, from February 2016 to end of May 2018, and we consider the resulting hourly measurements of easterly and northerly velocity components at depths 4 m, 10 m, 16 m, 22 m, 28 m and 34 m below the surface. At Salatskjæra, the buoy deployment lasted approximately 1.5 years, from March 2016 to September 2017, and we consider the same depths as for Munkskjæra, apart from depth 34 m which was left out as the acoustic measurements here appeared to be (occasionally) affected by the proximity to the seabed. The reason for focusing on the upper part of the water column is primarily a consequence of the measurement setup. In addition, the considered sites are located in an important area for fish farming (mainly Salmon farmed in open sea-cages). Knowledge of the current velocity as a function of depth during extreme events in the upper part of the water column is important both for structural design of the cages and for the welfare of the fish.

An essential point when relying on measurements is their quality and validity. The performance of acoustic Doppler current profilers in laboratory flumes is generally found to be good for measuring mean current velocity profiles, particularly in flow with low turbulence (Nystrom et al., 2007). However, in a recent 5-year measurement program in the North Sea, large discrepancies were observed between overlapping current speed data measured by different current profilers at the same locations and water depths, suggesting that the accuracy of current profilers is not as good as the user expects; see Bruserud and Haver (2017). Also, as our measurements are performed with ADCPs mounted on surface buoys, an aspect likely to affect of their validity is the presence of surface waves (an effect which is hoped to be 'averaged out' over the ensemble interval). There is only a limited literature investigating the effect of wave-induced motions on buoy-mounted ADCPs (see Mayer et al. (2007), Seim and Edwards (2007), Bruserud and Haver (2017), Lohrmann (1998) and Winant et al. (1994)). The overall conclusion is that the buoy motion does affect the measurements, but the above references do not agree on the magnitude of the effect. The latter is not really surprising considering that the buoy response depends on multiple factors such as buoy type, mooring system, wave conditions (including Stokes drift; see, e.g., Röhrs et al. (2012) and Longuet-Higgins (1953)) and ambient (Eulerian) current. This will not be discussed further; however, we emphasize that any statistical method assumes the input data to be valid. The corresponding validity of the estimated extremes therefore depends critically on the quality of the measurements.

3. Pre-processing of the data

Prior to the statistical modelling, pre-processing of the current velocity data is required. Although the techniques used are standard within the oceanographic community (Boon, 2004), they may not be familiar to an ocean engineer working with structural design. For completeness, we therefore provide some level of detail in the present section. Specifically, the mathematical techniques *principal component analysis* (PCA) and *harmonic analysis* is introduced, along with their application. We mention that, as presented here, the order of application of the two techniques is interchangeable.

3.1. Principal component analysis — resolving the current velocity into major and minor axis components

Principal component analysis (PCA), sometimes referred to as empirical orthogonal functions (EOF), is a statistical approach where the usual objective is to condensate the information contained in a large number of (interrelated) original variables into a smaller set of linearly uncorrelated variates with a minimal loss of information (in terms of variance); see Jolliffe (2002). This technique has been used for decades by oceanographers and meteorologists to analyse complex time series (Forristall and Cooper, 1997). In our case, the motivation for applying PCA is primarily to obtain *uncorrelated* current components at each depth, following Jonathan et al. (2012), not to reduce the dimensionality of the problem (unless the current to be analysed

is rectilinear). Note that uncorrelated variables are *not* necessarily statistically independent.

Consider a time series consisting of n measured horizontal current velocities at a given depth, expressed as orthogonal vector components $\mathbf{u}_e$ and $\mathbf{u}_n$; $u_{e,k}$ and $u_{n,k}$, $k = 1, \ldots, n$, being the velocity observed at time t_k in the eastward and northward direction, respectively. We now want to apply PCA to convert this set of (generally correlated) variables into a set of values of linearly uncorrelated variables, the *principal components*. This is achieved by using an orthogonal transformation, defined in such a way that the first principal component has the greatest fraction possible of the total variance and, consequently in the two-dimensional case, the second principal component has the least. The practical procedure for obtaining the principal components is as follows:

Our time series of horizontal current velocities is expressed as a $n\times2$ data matrix $\mathbf{U} = \begin{bmatrix}\mathbf{U}_e & \mathbf{U}_n\end{bmatrix}$, where $\mathbf{U}_e$ and $\mathbf{U}_n$ are the eastward and northward velocity vectors with *their mean value subtracted*. The sample covariance matrix $\mathbf{S}$ is then given as

$$\mathbf{S} = \frac{1}{n-1}\mathbf{U}^{\mathrm{T}}\mathbf{U} \tag{1}$$

where the diagonal elements of $\mathbf{S}$ is the variance of $\mathbf{u}_e$ and $\mathbf{u}_n$, respectively.

To find the principal components, we must calculate the eigenvalues and corresponding eigenvectors of $\mathbf{S}$. The resulting 2×2 unit eigenvector matrix, $\mathbf{V}$, is then sorted so that the first column of $\mathbf{V}$ is the eigenvector corresponding to the largest eigenvalue. The first principal component axis then simply refers to the first column of $\mathbf{V}$ and the second principal axis to the second column. The values, or scores, of the original variables onto the principal axes are then found as

$$\begin{bmatrix}\mathbf{u}_M & \mathbf{u}_m\end{bmatrix} = \begin{bmatrix}\mathbf{u}_e & \mathbf{u}_n\end{bmatrix}\mathbf{V} \tag{2}$$

where $\mathbf{u}_M$ is termed the *major axis component* and $\mathbf{u}_m$ is termed the *minor axis component*, corresponding to the first and second principal component, respectively.

In practice, $\mathbf{V}$ in Eq. (2) is nothing more than a rotation matrix. This is seen in Fig. 3 and 4, showing the resulting major and minor axis of the surface current velocity observations at Munkskjæra and at Salatskjæra. The dominant current direction is seen to be closely aligned with the east–west axis at Munkskjæra and in the southeast–northwest direction at Salatskjæra. The direction of the highest observed velocities at Salatskjæra is however not aligned with the major axis. The choice of positive directions is up to the analyst to decide; our choice is indicated in the figures.

The procedure above has been followed to resolve the current velocity into uncorrelated major and minor axis components independently at each depth at the two considered sites. At the Munkskjæra site, the major axis component account for 90 – 95% of the total current velocity variance, increasing with depth as shown in Fig. 5(a). In Fig. 5(b), it is seen that the relative major axis variance is less prominent at Salatskjæra, where it accounts for 75 – 85% of the total variance. The direction of the major axis is determined by the local bathymetry and topography at both locations. A slight anti-clockwise and clockwise rotation for increasing depths is seen at Munkskjæra and Salatskjæra, respectively.

Here, the direction of the major and minor axes has been decided based on the total current velocity at each depth, following Jonathan et al. (2012). Other rational choices exists, however — for instance deciding their direction based on the residual current velocity at each depth and/or only considering velocities whose magnitude exceeds some threshold. The best choice is dependent on the data at hand.

3.2. Harmonic analysis — decomposing the total current into tidal and residual currents

The measured total current velocity is the vector sum of an essentially deterministic tidal current and a stochastic (random) residual current. It is only meaningful to perform extreme value analysis on stochastic variables, so it would be desirable to decompose the observed current into a tidal and a residual component at each depth. The standard method for extracting the tidal signal from a time series is called *harmonic analysis* and will be briefly described in the following.

Unlike many other time signals in nature, tides and tidal currents are forced oscillations that occur only at known tidal frequencies (Boon, 2004). The driving forces originate from the gravitational fields of the sun and moon, acting on a rotating earth, expressed mathematically

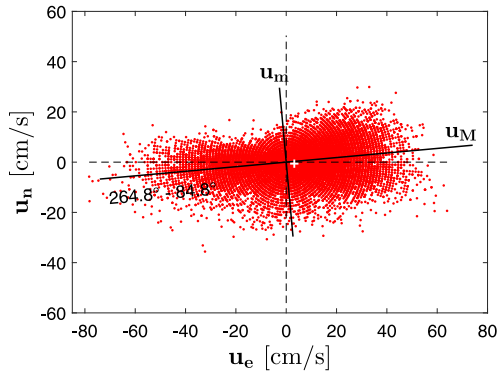

Fig. 3. Current velocity at 4 m depth at Munkskjæra. The (positive) major and minor axis resulting from application of PCA are indicated. The white cross is the bivariate mean, revealing a net surface flow in the eastward direction.

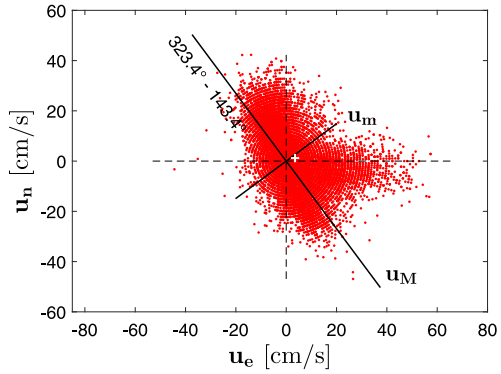

Fig. 4. Current velocity at 4 m depth at Salatskjæra. The (positive) major and minor axis resulting from application of PCA are indicated. The white cross is the bivariate mean, revealing a net surface flow in the northeastward direction.

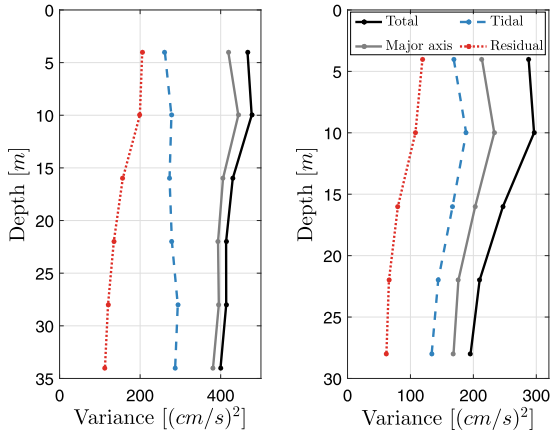

(a) Munkskjæra. (b) Salatskjæra.

Fig. 5. Total, major axis, tidal, and residual current velocity variance with depth.

as the tidal potential (Doodson, 1921). This astronomical forcing can be written as a linear combination of sinusoidal terms, each having a distinct amplitude, phase and temporal frequency (Foreman and Henry, 1989). The oceanic response can be described in the same manner, each sinusoid being referred to as a *tidal constituent*. Due to the hydrodynamic effects caused by irregular coastal boundaries and the bathymetry of the oceans, the amplitudes and phases of the constituents can vary greatly, but their frequencies remain the same as those in the tidal potential (Foreman and Henry, 1989). The tidal frequencies are all linear combinations of the rates of change of the mean lunar time (the earth rotation with respect to the moon) and five astronomical variables that uniquely specify the position of the sun and moon; see Foreman et al. (2009).

Unlike spectral analysis, harmonic analysis takes advantage of the fact that the tidal frequencies are known in advance. Once a suitable set of m tidal constituents has been chosen, the amplitude and phase of each constituent are calculated by solving a system of linear equations. In the one-dimensional case, this equation system takes the form

$$h(t_k) = A_0 + \sum_{j=1}^{m} A_j \cos\left(\sigma_j t_k - \phi_j\right) \tag{3}$$

where A_0 is the mean, A_j, ϕ_j and σ_j are the amplitude, phase and frequency of constituent j, and $h(t_k)$, $k = 1, \ldots, n$, is the observation at time t_k. Eq. (3) is generally overdetermined (there exists more equations than unknowns), and is therefore solved by a least squares technique, minimizing the equation residuals.

The UTide MATLAB functions by Codiga (2011), have been applied for the harmonic analysis of the current velocity at each depth. The functions take orthogonal current components along the first and second axes in any right-handed coordinate system as input; conventionally the eastward and northward components. The time series are permitted to be irregularly sampled and/or contain gaps. UTide then uses a refined two-dimensional, complex version of Eq. (3) to (indirectly) solve for the so-called *current ellipse parameters*. The tip of the velocity vector of a constituent traces out an ellipse over its tidal period, so the goal is to find the lengths of its semi-major and semi-minor axes, its angle of inclination and (Greenwich) phase; see, e.g., Foreman (2004) for illustrative figures. The equation system can be solved either by the ordinary least squares (OLS) method or by an iteratively reweighted least squares (IRLS) method, the latter limiting the sensitivity to outliers and reducing confidence intervals compared to the OLS method (Codiga, 2011). Diagnostics to assess constituent independence includes, among others, the conventional Rayleigh criterion (a time series of length T is required to distinguish between two constituents with frequency separation of T^{-1}) and its noise-modified version due to Munk and Hasselmann (1964), accounting for the amount of non-tidal energy (noise) in the record. The so-called nodal/satellite and astronomical argument corrections are evaluated at the exact times of each measurement, removing the restriction that the analysis periods should not be much longer than one year (Foreman et al., 2009). The nodal/satellite corrections accounts for the fact that the amplitudes and phases of the constituents are generally not constant due to interaction with minor unresolved constituents (called satellites), while the astronomical argument simply re-expresses phase lags with respect to an absolute time and space origin (Foreman and Henry, 1989).

There are a maximum of 146 possible tidal constituents that can be included in UTide. Of these, 45 are astronomical in origin while the remaining 101 are *shallow water tides*. The latter constituents arise due to distortion of the tidal wave by shallow water effects, and have frequencies that are multiples, sums and differences of the frequencies of the astronomical constituents (see, e.g., Pugh and Woodworth (2014) for further details). The automated decision tree constituent selection method (default option in UTide) due to Godin (1972) and formalized by Foreman (1977), was applied to decide which constituents to include in the analysis. The method selected a total of 68 constituents for inclusion in the harmonic analysis at both Munkskjæra and Salatskjæra.

Table 1
Current ellipse parameters of the five most energetic tidal constituents at the Munkskjæra and Salatskjæra sites at depth 4 m. The constituent period is given in solar hours. L_{maj} and L_{min} is the length of the semi-major and semi-minor axis. Positive and negative L_{min} means anticlockwise and clockwise rotation, respectively. θ is the semi-major axis inclination, measured anticlockwise from the positive eastward axis, and g is the Greenwich phase.

Constituent	Period [h]	L_{maj} [cm/s]	L_{min} [cm/s]	θ [deg]	g [deg]
Munkskjæra					
M_2	12.42	18.8	−0.79	4.23	233
S_2	12.00	6.98	−0.51	4.85	273
Sa	8766	6.33	0.46	19.6	318
N_2	12.66	3.83	−0.14	4.41	212
MSf	354.4	3.52	0.11	11.8	239
Salatskjæra					
M_2	12.42	15.7	−2.74	125	25.6
S_2	12.00	5.13	−1.14	121	60.1
N_2	12.66	3.05	−0.51	118	2.16
Sa	8766	2.34	−0.81	35.0	355
K_2	11.97	1.48	0.26	122	40.1

The resulting current ellipse parameters of the five most energetic tidal constituents are given in Table 1 for both sites. The tidal current at Munkskjæra and Salatskjæra is semidiurnal, dominated by the M_2 (principal lunar semidiurnal) and S_2 (principal solar semidiurnal) constituents. The seasonal, low-frequency constituent Sa (solar annual) is also seen to be important, particularly at Munkskjæra. It should be noted that this low-frequency constituent is largely influenced by non-tidal forcing (Boon, 2004).

Once the current ellipse parameters have been obtained, UTide can be used to reconstruct/hindcast the tidal current over the period of observations. In the reconstruction, we conservatively neglect non-significant tidal constituents having a signal-to-noise ratio (SNR) below 2 with respect to the raw signal at that frequency (default option in UTide; see Codiga (2011)). The residual current in the major and minor axis direction at depth i are then given as

$$\begin{aligned} u_{RM,i}(t_k) &= u_{M,i}(t_k) - u_{TM,i}(t_k) \\ u_{Rm,i}(t_k) &= u_{m,i}(t_k) - u_{Tm,i}(t_k) \end{aligned} \tag{4}$$

where subscript R refers to the residual current and T to the tidal current (the latter includes the mean current velocity). If the eastward and northward velocity components have been used as input to the harmonic analysis, the velocities are easily transformed to components along the major and minor axis at each depth using Eq. (2).

The decomposition of the total current into tidal and residual current is shown in Fig. 6 and 7 for the major axis surface current at Munkskjæra and Salatskjæra, respectively. Though only a 14-day period is plotted, it is clear that the tidal current is important at both locations. This is confirmed in Fig. 5, displaying the total, tidal, and residual current velocity variance with depth at the considered locations. The tidal current accounts for 57 – 71% of the total variance at Munkskjæra and 59 – 68% of the total variance at Salatskjæra. Accordingly, the variance of the current we are to perform extreme value analysis on (the residual current) is reduced by the same percentages. At both locations the relative importance of the residual current increases towards the sea surface. It is somewhat surprising to note that the total current variance at the top bin (4 m) is slightly lower than that at 10 m at both locations. When comparing buoy-mounted and bottom-mounted ADCPs, Mayer et al. (2007) found that the near-surface measurements of the buoy-mounted ADCPs were biased low. Though we have no means of verifying it, this could be a possible explanation for the observed near-surface velocity reduction in our measurements as well.

In the remaining sections, the tidal current is assumed to be deterministic and known at any time due to the preceding harmonic analysis.

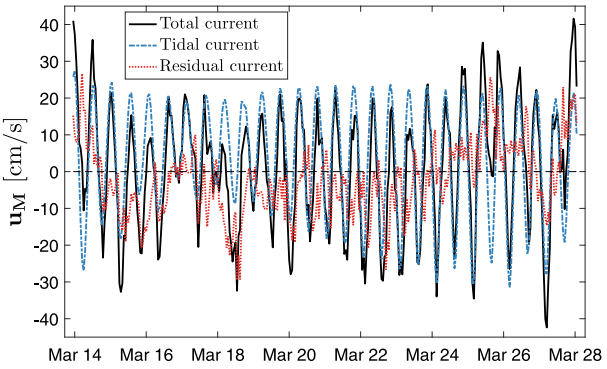

Fig. 6. 14-day plot of the major axis current velocity at Munkskjæra at depth 4 m and the resulting decomposition into tidal and residual current by harmonic analysis, March 2016. The 14.8-day spring-neap cycle can be observed in the tidal signal.

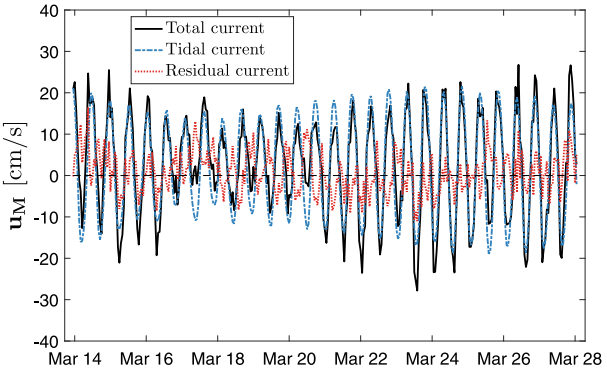

Fig. 7. 14-day plot of the major axis current velocity at Salatskjæra at depth 4 m and the resulting decomposition into tidal and residual current by harmonic analysis, March 2016. The 14.8-day spring-neap cycle can be observed in the tidal signal.

It is worth noting that an underlying assumption in tidal harmonic analysis is that the tide is stationary. There are cases where this assumption can be invalid; for instance as a result of nonlinear interaction between the tide and storm surges in shallow water, for internal tidal currents that change with the stratification, or seasonally varying ice cover that can modify both tidal elevation and current harmonics (Foreman et al., 2009). In such cases, the use of wavelet analysis, allowing for tidal non-stationarity, can provide a better alternative for extracting the tidal signal (see, e.g., Flinchem and Jay (2000)).

4. The conditional extremes model

In this section, a general description of the conditional extremes model by Heffernan and Tawn (2004) is given. For additional theoretical details, the reader should consult the original paper (Heffernan and Tawn, 2004) or the article by Heffernan and Resnick (2007), the latter providing a formal mathematical framework. Its application for joint modelling of extreme residual currents, including practical details and required modifications, in addition to the marginal modelling, is presented in Section 5.

Consider a continuous d-dimensional random vector variable $\mathbf{X} = (X_1, \ldots, X_d)$ with unknown distribution function $F(\mathbf{x})$; $\mathbf{X}$ being for instance simultaneously observed values of an environmental parameter at different locations. From a sample of n independent and identically distributed observations from F, the conditional extremes model by Heffernan and Tawn concerns the estimation of functionals of the distribution of $\mathbf{X}$ when $\mathbf{X}$ is extreme in at least one component. Specifically, it describes the conditional distribution of $\mathbf{X}_{-i}|X_i > v_{X_i}$, where $\mathbf{X}_{-i}$ denotes the vector variable $\mathbf{X}$ excluding component X_i and v_{X_i} is a high threshold. Here and throughout, vector algebra is to be interpreted componentwise.

4.1. Marginal transformation

Having established the marginal distribution of each X_i, $i = 1, \ldots, d$, by univariate extreme value theory (see Section 5.2), the method starts by componentwise transforming all variables to follow a common distribution. This is known as marginal standardization, and is performed in order to separate the marginal behaviour from the dependence structure between the components (Drees and Janßen, 2017). Heffernan and Tawn chose the standard Gumbel distribution for this purpose. We will however follow Keef et al. (2013), transforming the marginals to standard Laplace distributions. The motivation for choosing the Laplace distribution is that the semiparametric regression model in Heffernan and Tawn (2004), used to characterize the behaviour of $\mathbf{Y}_{-i}$ occurring with large Y_i, takes different functional forms for positively and negatively associated variables. As the Laplace distribution has both exponential tails and symmetry, this captures the exponential upper tail of the Gumbel distribution required for modelling positive dependence, while the symmetry allows the same functional form to be used for modelling the dependence of negatively associated variables (Keef et al., 2013). We will later see that this is particularly convenient for modelling current profiles as it generally includes modelling of both positively and negatively dependent variables.

Using the probability integral transform, our original vector variable $\mathbf{X}$ with marginal cumulative distributions $F_{X_i}(X_i)$, is thus transformed componentwise as

$$Y_i = \begin{cases} \log\{2F_{X_i}(X_i)\} & \text{for } X_i < F_{X_i}^{-1}(0.5) \\ -\log\{2[1 - F_{X_i}(X_i)]\} & \text{for } X_i \geq F_{X_i}^{-1}(0.5) \end{cases} \tag{5}$$

where $F_{X_i}^{-1}(q)$ is the inverse cumulative distribution function (quantile function) of X_i evaluated at the cumulative probability q. The new vector variable $\mathbf{Y} = (Y_1, \ldots, Y_d)$ then has standard Laplace distributed marginals with

$$\Pr\left(Y_i \leq y\right) = F_{Y_i}(y) = \begin{cases} \frac{1}{2}\exp(y) & \text{if } y < 0 \\ 1 - \frac{1}{2}\exp(-y) & \text{if } y \geq 0 \end{cases} \tag{6}$$

meaning that both the upper and lower tails of Y_i are exactly exponentially distributed. For clarity, $\mathbf{X}$ and $\mathbf{Y}$ are used throughout the paper to denote the variable with its original marginal distributions and with Laplace marginals, respectively, following Heffernan and Tawn (2004).

The focus will now be placed on extremal dependence modelling of variables with Laplace marginal distributions.

4.2. Dependence model

The dependence model considers the asymptotic structure of the conditional distribution $\Pr\left(\mathbf{Y}_{-i} \leq \mathbf{y}_{-i} \mid Y_i = y_i\right)$, arising from a d-dimensional random variable $\mathbf{Y} = (Y_1, \ldots, Y_d)$ with Laplace marginal distributions. $\mathbf{Y}_{-i}$ denotes the vector variable $\mathbf{Y}$ excluding component Y_i.

To examine the limiting conditional distributions as $y_i \to \infty$, the growth of $\mathbf{y}_{-i}$ must be controlled according to its dependence on Y_i so that the limiting distribution has non-degenerate marginals. This is achieved by assuming that for a given i, there exist vector normalizing functions $\mathbf{a}_{|i}(y_i)$ and $\mathbf{b}_{|i}(y_i)$ of the same dimension as $\mathbf{Y}_{-i}$, such that, for all fixed $\mathbf{z}_{|i}$,

$$\lim_{y_i \to \infty}\left[\Pr\left\{\frac{\mathbf{Y}_{-i} - \mathbf{a}_{|i}(y_i)}{\mathbf{b}_{|i}(y_i)} \leq \mathbf{z}_{|i} \mid Y_i = y_i\right\}\right] = G_{|i}(\mathbf{z}_{|i}) \tag{7}$$

where the limit distribution $G_{|i}$ has non-degenerate marginal distributions $G_{j|i}$ for all $j \neq i$.

Eq. (7) is assumed to hold exactly for all values of $Y_i > u_{Y_i}$ for a suitably high threshold u_{Y_i}. As a consequence, the random variable $\mathbf{Z}_{|i}$, defined by

$$\mathbf{Z}_{|i} = \frac{\mathbf{Y}_{-i} - \mathbf{a}_{|i}(y_i)}{\mathbf{b}_{|i}(y_i)}, \tag{8}$$

is independent of Y_i for $Y_i > u_{Y_i}$ and has distribution function $G_{|i}$. The extremal dependence behaviour is then characterized by location and scale functions $\mathbf{a}_{|i}(y_i)$ and $\mathbf{b}_{|i}(y_i)$ and the distribution function $G_{|i}$.

Due to the transformation to Laplace marginals, the form of the normalizing functions $\mathbf{a}_{|i}(y_i)$ and $\mathbf{b}_{|i}(y_i)$ falls into a simple parametric family, both for positively and negatively associated variables, given by

$$\begin{aligned}\mathbf{a}_{|i}(y_i) &= \boldsymbol{\alpha}_{|i} y_i \\ \mathbf{b}_{|i}(y_i) &= y_i^{\boldsymbol{\beta}_{|i}}\end{aligned} \tag{9}$$

where the vector constants $\boldsymbol{\alpha}_{|i}$ and $\boldsymbol{\beta}_{|i}$ have components $\alpha_{j|i} \in [-1, 1]$ and $\beta_{j|i} \in (-\infty, 1)$ for all $j \neq i$. No such simple class of parametric models exists for $G_{|i}$ as no specific structure is imposed by the limiting operation (7). $G_{|i}$ is therefore modelled nonparametrically.

The resulting dependence model is a multivariate semiparametric regression model of the form

$$\mathbf{Y}_{-i} = \boldsymbol{\alpha}_{|i} y_i + y_i^{\boldsymbol{\beta}_{|i}} \mathbf{Z}_{|i} \quad \text{for } Y_i = y_i > u_{Y_i} \tag{10}$$

where $i = 1, \ldots, d$. For a large value of Y_i, the behaviour of the remaining components in $\mathbf{Y}$ is thus described by Eq. (10). The constant $\alpha_{j|i}$ describes the strength of dependence between Y_j on large values of Y_i, while $\beta_{j|i}$ describes how the variability of Y_j changes with increasing Y_i. Positive and negative values of $\alpha_{j|i}$ corresponds, respectively, to positive and negative association between the variables (Y_i, Y_j). Positive $\beta_{j|i}$ means that the variance of Y_j increases as Y_i increases, whereas negative $\beta_{j|i}$ means that the variance decrease. For $\alpha_{j|i} = 1$ and $\beta_{j|i} = 0$, (Y_i, Y_j) are said to be asymptotically (positive) dependent (the quantiles of the distribution of $Y_j|Y_i = y_i$ grows at the same rate as y_i for $y_i \to \infty$), and for $\alpha_{j|i} = -1$ and $\beta_{j|i} = 0$, they are asymptotically negative dependent; otherwise they are asymptotically independent (see, e.g., Keef et al. (2013)).

4.3. Inference

As stepwise estimation is generally simpler than joint estimation, inference for marginal and dependence structure is undertaken stepwise in Heffernan and Tawn (2004). First, the parameters of the marginal distributions of the components of $\mathbf{X}$ are estimated. After transformation to Laplace marginals, the dependence parameters are estimated assuming that the marginal parameters are known. Since the conditional extremes model by Heffernan and Tawn offers nothing new regarding marginal inference, we focus here on the estimation of the conditional model parameters.

Inference for the parametric part of the conditional model consists of estimating the values of the vector constants $\boldsymbol{\alpha}_{|i}$ and $\boldsymbol{\beta}_{|i}$ based on the sample data. During inference, a parametric model for $G_{|i}$ must be assumed. Specifically, the components of $\mathbf{Z}_{|i}$ are (falsely) assumed to be mutually independent and Gaussian distributed. The Gaussian distribution was selected for its simplicity and superior performance (Heffernan and Tawn, 2004). If $\mathbf{Z}_{|i}$ has marginal means and standard deviations denoted by the vectors $\boldsymbol{\mu}_{|i}$ and $\mathbf{s}_{|i}$, then, following Eq. (10), the means and standard deviations of the random variables $\mathbf{Y}_{-i}|Y_i = y_i$, for $y_i > u_{Y_i}$, are $\boldsymbol{\alpha}_{|i} y_i + \boldsymbol{\mu}_{|i} y_i^{\boldsymbol{\beta}_{|i}}$ and $\mathbf{s}_{|i} y_i^{\boldsymbol{\beta}_{|i}}$, respectively. From the $k = 1, \ldots, n_{u_{Y_i}}$ observations of $\mathbf{Y}|Y_i > u_{Y_i}$, the maximum likelihood estimates of the unknown parameters $\boldsymbol{\alpha}_{|i}$, $\boldsymbol{\beta}_{|i}$, $\boldsymbol{\mu}_{|i}$ and $\mathbf{s}_{|i}$ are then found from the following objective function (log-likelihood):

$$\begin{aligned} Q_{|i}\left(\boldsymbol{\alpha}_{|i}, \boldsymbol{\beta}_{|i}, \boldsymbol{\mu}_{|i}, \mathbf{s}_{|i}\right) = -\sum_{j \neq i} \sum_{k=1}^{n_{u_{Y_i}}} \Bigg[& \log\left\{ s_{j|i} y_{i|i,k}^{\beta_{j|i}} \right\} \\ & + \frac{1}{2}\left\{ \frac{y_{j|i,k} - \left(\alpha_{j|i} y_{i|i,k} + \mu_{j|i} y_{i|i,k}^{\beta_{j|i}}\right)}{s_{j|i} y_{i|i,k}^{\beta_{j|i}}} \right\}^2 \Bigg] \end{aligned} \tag{11}$$

Numerical maximization of $Q_{|i}$ over the parameter space of the model is required to obtain the point estimates $(\hat{\boldsymbol{\alpha}}_{|i}, \hat{\boldsymbol{\beta}}_{|i}, \hat{\boldsymbol{\mu}}_{|i}, \hat{\mathbf{s}}_{|i})$, with $\boldsymbol{\mu}_{|i}$ and $\mathbf{s}_{|i}$ treated as nuisance parameters. The distribution $G_{|i}$ is finally estimated nonparametrically by using the empirical distribution function $\hat{G}_{|i}$ of replicates of the random variable $\hat{\mathbf{Z}}_{|i}$, defined by

$$\hat{\mathbf{Z}}_{|i} = \frac{\mathbf{Y}_{-i} - \hat{\boldsymbol{\alpha}}_{|i} Y_i}{Y_i^{\hat{\boldsymbol{\beta}}_{|i}}} \quad \text{for } Y_i = y_i > u_{Y_i} \tag{12}$$

The resulting observations $\hat{\mathbf{z}}_{|i}$ provide a sample from the multivariate distribution $G_{|i}$.

A problem identified by Keef et al. (2013) is that due to the omission by Heffernan and Tawn of imposing joint constraints on the parameters of the semiparametric regression model ($\alpha_{j|i}$ and $\beta_{j|i}$) and the nonparametric element of the model, inconsistencies with the marginal distributions can arise. The strongest form of extremal dependence between two variables is asymptotic dependence (Coles et al., 1999), given by $(\alpha_{j|i}, \beta_{j|i}) = (1, 0)$ in the dependence model (10). This suggests that when $\alpha_{j|i} = 1$, $\beta_{j|i}$ cannot be positive. However, as the parameter space is $(\alpha_{j|i}, \beta_{j|i}) \in [-1, 1] \times (-\infty, 1)$, such a combination of parameters is allowed in the original model. This, together with the nonparametric element of the model, results in the possibility of the estimated joint probabilities to exceed the marginal probabilities. To avoid this, it is recommended to impose the constraints given in Keef et al. (2013) on $\alpha_{j|i}$ and $\beta_{j|i}$ if strong extremal dependence is expected between the variables. For pairs (Y_i, Y_j), these constraints follows from requiring a stochastic ordering, assuring that conditional quantiles for any form of asymptotic independence are not larger than under asymptotic positive dependence, nor smaller than under asymptotic negative dependence. These constraints are imposed only on extrapolations (i.e. for $y_i > v$ where v is a value above the maximum observed value of Y_i). The reader is referred to Keef et al. (2013) for further details.

4.4. Conditional simulation

Since the dependence model (10) is semiparametric, estimates for various extremal statistics must be acquired by simulation. We thus generate random samples of $\mathbf{X}|X_i > v_{X_i}$, where $v_{X_i} \geq F_{X_i}^{-1}\left(F_{Y_i}\left(u_{Y_i}\right)\right)$, for each i using the estimated conditional models. From these samples, Monte Carlo approximations of functionals of the joint tails of the distribution of $\mathbf{X}$ can then be obtained. The sampling algorithm for each i is as follows:

1. Simulate Y_i from a Laplace distribution conditional on it exceeding its cumulative probability corresponding to $F_{X_i}(v_{X_i})$.
2. Sample $\mathbf{Z}_{|i}$ from $\hat{G}_{|i}$ independent of Y_i.
3. Obtain $\mathbf{Y}_{-i} = \hat{\boldsymbol{\alpha}}_{|i} Y_i + Y_i^{\hat{\boldsymbol{\beta}}_{|i}} \mathbf{Z}_{|i}$.
4. Transform $\mathbf{Y} = (\mathbf{Y}_{-i}, Y_i)$ to $\mathbf{X}$ using the inverse of transformation (5).

Let us say that we from the data sample at hand have n independent observations of $\mathbf{X}$ where $\mathbf{X}$ is extreme in at least one component. A simulated random realization of this process, covering the same period, is then obtained by simulating n pseudo-observation of $\mathbf{X}$ by the sampling algorithm above. Typically, many of the observed $\{\mathbf{x}_k\}_{k=1}^n$ comprises observations where more than one of the components $x_{i,k}$ are simultaneously extreme. This raises the question of how to determine the number of times one should condition on each X_i to obtain $\mathbf{X}_{-i}$ for all $i = 1, \ldots, d$, resulting in a total of n simulated pseudo-observations of $\mathbf{X}$. In the proceeding simulation of residual current profiles, we principally follow the procedure proposed by Jonathan et al. (2012) to estimate this.

The main argument in Jonathan et al. (2012) is that since the conditional extremes model is motivated asymptotically, it is most appropriately applied to the conditioning variable whose value is most extreme in its marginal distribution. Transformed to $\mathbf{Y}$, this means that for the observations $\{\mathbf{y}_k\}_{k=1}^n$, the number of times to condition on variable Y_i during the conditional simulation, is determined by

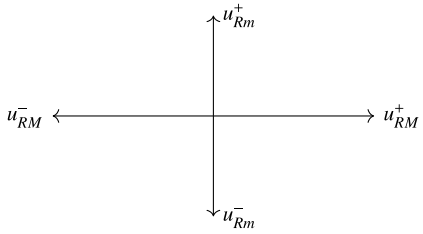

Fig. 8. Illustration of the four residual current velocity components in the local coordinate system defined by the major and minor axis at each depth.

the number of times which Y_i was the largest component of $\{\mathbf{y}_k\}_{k=1}^n$. The rate at which to condition on each Y_i (or X_i) is thus found as $\frac{1}{n}\sum_{k=1}^n \mathbf{1}\{y_{i,k} = \max \mathbf{y}_k\}$, where $\mathbf{1}\{A\}$ denotes the indicator function of some event A. In Section 5.4, a slight modification of this procedure is described — the modification being introduced to account for temporal dependence.

5. Application

In this section, the statistical modelling of the residual current components is described in detail and applied to obtain extreme vertical residual and total current profiles at the two considered locations (Munkskjæra and Salatskjæra). This includes modelling the complete marginal distribution (bulk and tail distribution) of each residual current component, characterizing the dependence structure between the components by application of the conditional extremes model (Heffernan and Tawn, 2004), and outlining the Monte Carlo procedure used to simulate extreme current velocity profiles. Following Pugh (1982), Robinson and Tawn (1997), Jonathan et al. (2012), the tidal and residual currents are assumed to be independent. Inspection of plots of observed residual currents against observed tidal currents from the measurements (as in Pugh and Vassie (1976)) confirmed that the independence assumption generally appears reasonable. Just as assuming tide–surge independence when estimating extreme sea-levels, this can however be a slightly conservative assumption in some cases, particularly in shallow water (see, e.g., Prandle and Wolf (1978), Horsburgh and Wilson (2007), and Pugh and Woodworth (2014)). Subsequent to the statistical modelling, extreme total current velocity profiles can then be obtained by randomly adding predicted tidal current profiles to realizations of extreme residual current profiles. We start by defining the considered residual current velocity components.

5.1. Residual current components

The directionality of the extreme currents needs to be accounted for in the analysis. This requires characterization of the extremal behaviour of both positive and negative principal current components. The observed residual current velocities are therefore split into four velocity components at each depth. Specifically, for each depth i we consider the positive major axis component $u^+_{RM,i}$, the negative major axis component $u^-_{RM,i}$, the positive minor axis component $u^+_{Rm,i}$, and the negative minor axis component $u^-_{Rm,i}$; see Fig. 8.

Since positive and negative velocity components along a given axis at a given depth are mutually exclusive events, one can only observe one of the major axis and one of the minor axis components simultaneously at each depth. In order to work with only positive variable values, the residual current velocity components for the $k = 1, \dots, n$ observations are defined as

$$\begin{aligned} u^+_{RM,ik} &= u_{RM,ik} \mid u_{RM,ik} > 0 \\ u^-_{RM,ik} &= -u_{RM,ik} \mid u_{RM,ik} < 0 \\ u^+_{Rm,ik} &= u_{Rm,ik} \mid u_{Rm,ik} > 0 \\ u^-_{Rm,ik} &= -u_{Rm,ik} \mid u_{Rm,ik} < 0 \end{aligned} \tag{13}$$

A velocity component is said to be *unobserved* if the condition in Eq. (13) is not fulfilled. Denoting the total number of residual current components d, an observed velocity profile thus contains $d/2$ observed velocity components and $d/2$ unobserved components. The total number of residual current components is equal to 24 at Munkskjæra and 20 at Salatskjæra. As the mean current velocity is included in the tidal current, the sample size of each residual current velocity component $u^{+/-}_{RM,i}$ and $u^{+/-}_{Rm,i}$ is expected to be approximately equal to $n/2$.

5.2. Marginal modelling

Marginal modelling is performed independently for each of the four residual current components $u^{+/-}_{RM}$ and $u^{+/-}_{Rm}$ at each depth. From now, we denote the full set of residual current components as $\{X_i\}_{i=1}^d = \left(u^+_{RM,1}, u^-_{RM,1}, u^+_{Rm,1}, u^-_{Rm,1}, u^+_{RM,2}, \dots\right)$ and refer to $u^{+/-}_{RM}$ and $u^{+/-}_{Rm}$ only when needed.

Since the aim is to describe all values of $\mathbf{X}_{-i}$ that can occur with any large X_i, a model for the complete marginal distribution F_{X_i} of each X_i is required. For this purpose, we essentially follow Heffernan and Tawn (2004), adopting the semiparametric model by Coles and Tawn (1991, 1994), which comprises the generalized Pareto distribution for X_i above a high threshold u_{X_i} and the empirical distribution function below the threshold (such models are sometimes referred to as *mixture models*). The empirical distribution function, describing the bulk of observations, is established based on all (hourly) observations below the threshold, while inference for the tail distribution is made by application of the peaks over threshold (POT) method to account for marginal temporal dependence at extreme levels. As the latter distribution refers to events (cluster maxima) rather than individual sequential observations, an approach is described to properly connect the 'all observation based' bulk distribution and the 'event based' tail distribution. Similar approaches have been used by for instance Mazas et al. (2014) in connection with estimation of extreme sea levels.

The marginal model of each residual current velocity component thus consists of:

1. A bulk distribution; describing observations below a high threshold by the empirical distribution function.
2. A tail distribution; identifying cluster maxima above the threshold by the peaks over threshold method and fitting these maxima to the generalized Pareto distribution.
3. Connecting the bulk and the tail distribution to obtain the complete marginal distribution.

Giving particular emphasis to the fitting of the tail distribution, the points above will be outlined in the current subsection.

5.2.1. Bulk distribution

Marginally, points below the threshold u_{X_i} are relatively dense, and are therefore well described by the empirical distribution function $\tilde{F}_{X_i}$, i.e.

$$\tilde{F}_{X_i}(x) = \frac{\text{num. elem. } \{\mathbf{x}_{i,k}\}_{k=1}^{n_{X_i}} \le x}{n_{X_i}} \quad \text{for } x \le u_{X_i} \tag{14}$$

where n_{X_i} is the number of observations of variable X_i. The denominator in the expression for $\tilde{F}_{X_i}$ is sometimes written $(n_{X_i} + 1)$, the difference being negligible here. The threshold u_{X_i} for each residual current velocity component, is decided as part of the fitting procedure for the tail distribution.

5.2.2. Tail distribution

From univariate extreme value theory, it can be shown that the generalized Pareto (GP) distribution arises as the limiting distribution for excesses over thresholds (Davison and Smith, 1990) — a result

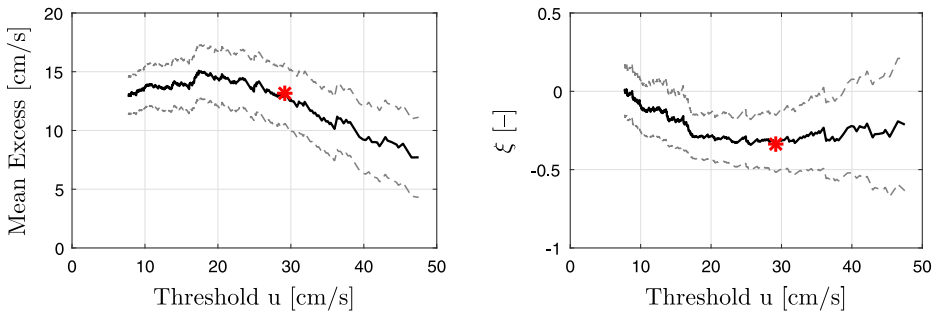

(a) Mean residual life plot. (b) Shape parameter stability plot.

Fig. 9. Illustrations of graphical diagnostics, here for u^{+}_{RM} at 22 m depth at Munkskjæra. The plotted threshold ranges from the 60% to the 99.5% quantile. Grey dashed lines are Wald type 95% confidence intervals. Red asterisks indicate the chosen threshold, corresponding to the 95% quantile.

originally due to Pickands (1975) and Balkema and de Haan (1974).[1] The justification for the generalized Pareto distribution as the limiting distribution for excesses over thresholds and subsequent parameter and return level estimates, are based on an assumption that the exceedances are *independent*. This is not a valid assumption for our hourly measured residual current velocities. Temporal dependence is clearly observed, particularly for the major axis velocity components, resulting in a tendency of extremes to cluster. However, if we introduce a condition that limits the dependence structure of the sequence, it can be shown that the maxima of (dependent) stationary series follows the same distributional limit laws as those for independent series (Leadbetter et al., 1983; Coles, 2001).

The peaks over threshold (POT) method with declustering is applied to limit marginal temporal dependence at extreme levels. Specifically, for exceedances above the threshold u_{X_i}, only the largest excess within a cluster of exceedances is considered; the *cluster peak excess*, or *cluster maxima*. The most common definition of clusters is as runs of consecutive exceedances, with an additional temporal separation criterion (Caires and Sterl, 2005). We define the cluster peak excesses simply as the highest peaks above the threshold with a minimum peak-to-peak separation of τ hours — a peak being defined as the highest observation of consecutive exceedances. This cluster peak excess definition is related to the runs method described in e.g. Smith and Weissman (1994), though we feel it is more convenient to impose the temporal separation criterion directly on the peaks rather than on the required 'below threshold time'. It should be mentioned that such definitions are often asymptotically equivalent (Leadbetter, 1991).

The marginal tail of X_i for $i = 1, \ldots, d$, describing the distribution of the independent cluster peak excesses $X_{C,i}$ conditional on $X_{C,i} > u_{X_i}$, is thus modelled by

$$G_{X_{C,i}}(x) = \begin{cases} 1 - \left(1 + \frac{\xi_i (x - u_{X_i})}{\sigma_i}\right)^{-1/\xi_i}_{+} & \xi_i \neq 0 \\ 1 - \exp\left(-\frac{(x - u_{X_i})}{\sigma_i}\right) & \xi_i = 0 \end{cases} \tag{15}$$

where u_{X_i} is a high threshold for X_i and ξ_i and σ_i are shape and scale parameters, respectively, with $\sigma_i > 0$ and the operator $(s)_+ = \max(s, 0)$. If $\xi_i < 0$, the distribution of excesses has an upper bound of $u_{X_i} - \sigma_i/\xi_i$, while for $\xi_i \geq 0$ the distribution as no upper limit. The case $\xi_i = 0$ is interpreted as the limit $\xi_i \to 0$, resulting in the exponential distribution with mean excess σ_i.

Before the parameters, (ξ_i, σ_i), of the generalized Pareto distribution can be estimated, a suitable threshold u_{X_i} and minimum peak-to-peak separation time τ_{X_i} have to be decided for each X_i. The minimum peak-to-peak separation time is usually set based on physical considerations (often related to typical storm durations for parameters causing environmental loads), while the threshold can be more difficult to decide. The issue of threshold selection amounts to a trade-off between bias and variance; too low a threshold is likely to violate the asymptotic basis of the model, leading to bias, while too high a threshold leads to fewer excesses with which the model can be estimated, leading to high variance (Coles, 2001).

We use the graphical diagnostics outlined by Coles (2001) and Scarrott and MacDonald (2012), in addition to the Anderson–Darling statistic, for deciding the threshold. The so-called mean residual life plot and the parameter stability plots are based on the fact that if the generalized Pareto distribution is valid for (cluster peak) excesses of the threshold u_0, it should also be valid for all thresholds $u > u_0$. These plots are obtained by calculating the mean of the cluster peak excesses $E(X - u \mid X > u)$ and estimating the GP parameters over a range of different thresholds. Above a threshold for which the generalized Pareto distribution is valid, the mean residual life plot and the scale parameter σ should be approximately linear in u, while the shape parameter ξ should be approximately constant. The scale parameter can alternatively be reparametrized as $\sigma^* = \sigma - \xi u$, so that σ^* should also be constant with u. The lowest threshold for which the above holds true, taking sample uncertainty into account, is then selected. We found (subjectively) the mean residual life plot and the shape parameter stability plot to be the most informal; see Fig. 9 for an illustration. Due to the large number of considered residual current components, a suitable common threshold corresponding to a given non-exceedance probability (as measured by $\tilde{F}_{X_i}(x)$) was selected; one threshold for all the major axis components and one for the minor axis components. The GP parameters were estimated by maximum likelihood – see, e.g., Grimshaw (1993) – though, several alternative methods exists (de Zea Bermudez and Kotz (2010a,b) and Mackay et al. (2011) are useful references in this respect).

Return level plots were used to validate the threshold choices and, more generally, the validity of the GP distribution. Such plots, where the estimated N-year return level is plotted against N, the latter on logarithmic scale, are particularly convenient since the effect of extrapolation is highlighted. For a given threshold and corresponding estimated GP parameters, the N-year return level for variable X_i, $x_{i,N}$, is given by

$$x_{i,N} = u_{X_i} + \frac{\sigma_i}{\xi_i}\left[\left(n_{Ci,1y} N\right)^{\xi_i} - 1\right] \tag{16}$$

Denoting the total number of observations by n, the theoretical possible number of (here, hourly) observations during a year by n_{1y} (= 8766) and the total number of observed cluster peak excesses of variable X_i by n_{Ci}, it follows that the estimated average number of cluster peak excesses per year for variable X_i, $n_{Ci,1y}$ in Eq. (16) is given by

$$n_{Ci,1y} = n_{Ci} \frac{n_{1y}}{n}$$

[1] Many practitioners within engineering disciplines use the Weibull distribution as an alternative (based on empirical goodness-of-fit to data); this is a credible candidate model for our data as well.

where n/n_{1y} is the effective number of years of measurements, and accounts for possible missing observations (gaps in the measured time series) assuming they are missing at random.

As the graphical diagnostics discussed above can be rather subjective and sometimes difficult to interpret, the Anderson–Darling statistic was used as an additional, objective goodness-of-fit test. This statistic is a modification of the Cramér–von Mises static, giving more weight to the tail of the distribution, making it particularly powerful for detecting tail discrepancies. We found it very convenient to use this statistic as a quick way of assessing the overall performance of the fitted marginal models, looking at the number of model rejections at the 5% significance level for a given choice of thresholds for all X_i. Plotting the calculated value of the Anderson–Darling statistic and the corresponding critical test value over a range of thresholds, for each X_i, was also helpful. Reference is made to Choulakian and Stephens (2001) for additional details regarding the Anderson–Darling statistic and critical test values for the generalized Pareto distribution.

An initial minimum peak-to-peak separation time τ of 30 h was selected for all variables before the diagnostics above were utilized to identify a suitable cumulative threshold for the major and minor axis components. The initial separation time was decided based on time series inspection and knowledge of typical storm durations in the area. In addition, it seemed rational to adopt a separation time larger than the period of the semidiurnal and diurnal tidal constituents so that dependence introduced due to possible tidal–residual current interaction and lack of fit of the harmonic model is limited (if inertial oscillations were important, the inertial period at the given latitude should probably be considered as well; see generally Wunsch (2015), Chap. 5). Using the initial τ, a threshold corresponding to the 95% quantile for the major axis components $u^{+/-}_{RM,i}$ and the 94% quantile for the minor axis components $u^{+/-}_{Rm,i}$ were found to give reasonably stable results at both locations. This is similar to that found by Robinson and Tawn (1997) and Jonathan et al. (2012) (both used the 95% quantile), though, strictly, the numbers are not directly comparable due to differences in the involved variables. A simple assessment of the threshold sensitivity on the estimated marginal extremes were made by plotting the estimated 50-year return level for some of the velocity components for a range of thresholds. These estimates were generally surprisingly stable for a broad range of (reasonable) threshold choices. This is reassuring, considering the subjectivity involved in the threshold selection process.

Having decided the threshold, the final peak-to-peak separation time was determined by considering different values of τ, ranging from 12–48 h, looking at the effect changes in τ had on the mentioned diagnostics (the return level plots were particularly informal in this context). As with the threshold choice, the issue is a trade-off between bias and variance. A minimum peak-to-peak separation time $\tau = 30$ hours gave the most stable results and was thus selected. However, the results were not particularly sensitive to the precise value of τ. This is in line with that reported in several other studies (Davison and Smith, 1990), such as by Tawn (1988) in the case of sea levels. With the final choice of thresholds and minimum peak-to-peak separation time, the fitted GP models passed the Anderson–Darling test at the 5% significance level for all X_i at both locations.

A representative illustration of the mean residual life and shape parameter diagnostics are shown in Fig. 9 for the u^{+}_{RM} velocity component at 22 m depth at Munkskjæra. Above the chosen threshold, indicated by the red asterisks, the mean residual life plot is seen to be approximately linear in u while the shape parameter is approximately constant, taking sampling variability into account (indicated by the confidence intervals). The maximum likelihood estimates of the GP parameters are given in Fig. 10(a) and 10(b) for all velocity components at Munkskjæra and Salatskjæra, respectively. The shape parameter is in most cases negative, indicating the existence of an upper limit for these residual current velocity components. The goodness-of-fit of the GP distribution and the effect of extrapolation is illustrated in the return level plot in Fig. 11, again for u^{+}_{RM} at 22 m depth at Munkskjæra. 95% confidence intervals based on profile likelihood are added (see, e.g., Coles (2001)); such intervals are usually more accurate than Wald type intervals. Important points to note are the asymmetric confidence intervals, reflecting the greater uncertainty about high values, and the large uncertainties that arises once the model is extrapolated to values well beyond the range of observations. With only 1.5–2.5 years of observations, large uncertainty will thus inevitably be associated with estimates of return levels corresponding to return periods ranging from 10–100 years, typically required for design. The estimated 10 and 50 year return values for all residual current components, including confidence intervals, are found in Table A.2 in the appendix, together with all relevant marginal distribution parameters. It is interesting to note the particularly wide confidence intervals seen for most of the velocity components with a high value of the GP shape parameter. Though, considering the physics of our problem, the most extreme intervals appears unrealistic — in such cases better estimates could probably be obtained by penalized maximum likelihood; see Coles and Dixon (1999).

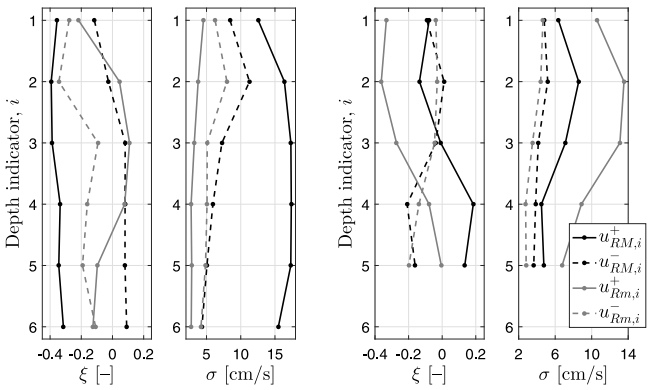

(a) Munkskjæra. (b) Salatskjæra.

Fig. 10. Maximum likelihood estimates of the GP shape (ξ) and scale (σ) parameters of the major ($u^{+/-}_{RM,i}$) and minor ($u^{+/-}_{Rm,i}$) axis components at Munkskjæra and Salatskjæra with depth. The estimates are based on a threshold corresponding to the 95% quantile for the major axis components, the 94% quantile for the minor axis components and a minimum peak-to-peak separation time $\tau = 30$ hours.

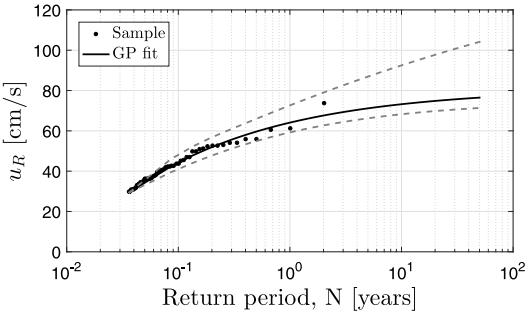

Fig. 11. Return level plot for the GP model fitted to cluster peak excesses of residual current component u^{+}_{RM} at 22 m depth at Munkskjæra. Grey dashed lines are 95% confidence intervals based on profile likelihood.

5.2.3. Connecting the bulk and tail distribution

The bulk distribution describes all (hourly) observations below the thresholds for each X_i, $i = 1, \ldots, d$, while the tail distribution describes only the independent cluster peak excesses above the threshold. For consistency below and above the threshold, it would therefore be favourable to transform the tail distribution into a distribution describing arbitrary (hourly) exceedances rather than just the cluster

maxima. This is further motivated by our aim of characterizing instantaneous current profiles — during an extreme event, simultaneously observed threshold-exceeding current components of the profile might not necessarily all correspond to (marginal) cluster peak excesses.

The goal is to transform the distribution of the independent cluster peak excesses into the distribution of dependent (hourly) sequential residual current velocities above the thresholds u_{X_i}, $i = 1, \ldots, d$. To transform the distribution of the independent cluster peak excesses into the distribution of all (hourly) excesses, it is necessary to introduce the so-called *extremal index*, θ, which lies in the interval $[0, 1]$ (see, e.g., Beirlant et al. (2004), Chavez-Demoulin and Davison (2012)). The extremal index has a physical and intuitively appealing interpretation due to Leadbetter (1983) as the inverse of the (limiting) mean cluster size. If $\theta = 1$, exceedances of an increasing threshold occur singly in the limit, while if $\theta < 1$, exceedances tend to cluster in the limit. The finite sample approximation of θ due to Tawn and Vassie (1989), θ_x, is an index varying with the level x. For large x, the physical interpretation of θ holds for θ_x, and its inverse can thus be calculated as

$$\hat{\theta}_x^{-1}(x) = \frac{\text{number of exceedances of } x}{\text{number of cluster maxima exceeding } x} \tag{17}$$

The above equation can however not be used to directly calculate $\theta_x^{-1}(x)$ for x beyond the range of the data, and the uncertainty of the empirical estimates of $\hat{\theta}_x^{-1}(x)$ increases for increasing x. Also, inevitably, $\hat{\theta}_x^{-1}(x) \to 1$ as x approaches the highest observation of the sample.

Denoting the extremal index obtained at the marginal threshold u as θ_u, Tawn (1990) notes that the distribution function of an arbitrary exceedance is influenced by the factor $\theta_u \theta_x^{-1}$. Following a similar notation as in Eastoe and Tawn (2012), conditional on $x > u$, we then have the following (subasymptotic) relation between quantiles of the distribution function of an arbitrary exceedance, $G_X(x)$, and that of an independent cluster peak excess, $G_{X_C}(x)$:

$$1 - G_X(x) = \theta_u \theta_x^{-1}(x) \left[1 - G_{X_C}(x)\right] \quad \text{given } x > u \tag{18}$$

θ_u can be interpreted as a scale factor to account for the increased sample size of all excesses relative to the cluster peak excesses, while $\theta_x^{-1}(x)$ accounts for the increased probability of observing an arbitrary exceedance above x due to dependence relative to if all exceedances above the level were independent cluster peak excesses.

The complete marginal distribution F_{X_i} of each X_i can thus be taken as

$$F_{X_i}(x) = \begin{cases} 1 - p_{u_{X_i}} \theta_{u_{X_i}} \theta_{x_i}^{-1}(x) \left[1 - G_{X_{C,i}}(x)\right] & \text{for } x > u_{X_i} \\ \tilde{F}_{X_i}(x) & \text{for } x \leq u_{X_i} \end{cases} \tag{19}$$

where $G_{X_{C,i}}(x)$ is the generalized Pareto distribution given by Eq. (15), $\tilde{F}_{X_i}(x)$ is the empirical distribution function, and $p_{u_{X_i}} = 1 - \tilde{F}_{X_i}(u_{X_i})$ is the probability of exceeding the threshold u_{X_i}.

Clearly, an estimate of $\theta_x^{-1}(x)$ is required beyond the range of the data. A rational approach would then be to estimate θ_x^{-1} by Eq. (17) at regularly spaced levels, fit a function to these estimates, and extrapolate. As commented in Tawn and Vassie (1989), the choice of an appropriate function is not immediately obvious, but results from extreme value theory (Leadbetter, 1983) suggest that in the limit, a *constant* is the correct function.

Denoting the (asymptotic) limiting extremal index θ_{lim} and the associated level x_{lim} for which $\theta_x(x) = \theta_{lim}$ for all $x \geq x_{lim}$, we have tested three different approaches for estimating θ_{lim} and x_{lim}, in addition to $\theta_x(x)$ on the intermediate range $u \leq x \leq x_{lim}$:

1. Simply take $\theta_x(x) = \theta_u$ for all $x \geq u$ (implying $\theta_{lim} = \theta_u$). From Eq. (18) it can be seen that this is equivalent to assuming that the distribution function of an arbitrary exceedance equals that of an independent cluster maxima.
2. Using an approach inspired by Mazas et al. (2014), taking $\theta_{lim} = 1$ and having $\theta_x^{-1}(x)$ varying linearly from θ_u^{-1} at $x = u$ to 1 at $x = x_{lim}$, where x_{lim} is the lowest level x for which Eq. (17) gives $\hat{\theta}_x^{-1} = 1$.
3. Following Tawn and Vassie (1989), estimating θ_x^{-1} by Eq. (17) at regularly spaced levels for $u \leq x \leq x_{max}$, where x_{max} is the highest observation, and using simple weighted least squares to estimate θ_{lim}^{-1}. The same approach can be used to estimate x_{lim}. We adopted the estimators

$$\hat{\theta}_{lim}^{-1} = \frac{\sum \sqrt{k_j} \hat{\theta}_x^{-1}(x_j)}{\sum \sqrt{k_j}} \tag{20}$$

$$\hat{x}_{lim} = \frac{\sum \sqrt{k_j} x_j}{\sum \sqrt{k_j}} \tag{21}$$

where k_j is the number of cluster maxima above the level x_j. On $u \leq x \leq \hat{x}_{lim}$, $\theta_x^{-1}(x)$ is taken to vary linearly between θ_u^{-1} at $x = u$ and $\hat{\theta}_{lim}^{-1}$ at $x = \hat{x}_{lim}$.

The resulting estimates of $\theta_x^{-1}(x)$ are displayed in Fig. 12(a) for residual current component u_{RM}^{+} at 4 m depth at Munkskjæra, highlighting the differences between the three considered approaches. In Fig. 12(b), using Eq. (19), the resulting survival function $\bar{F}(x) = 1 - F(x)$ is plotted against the empirical 'all observation' estimates. In line with results in Eastoe and Tawn (2012), approach 1 fits the empirical estimates poorly, overpredicting the probability of exceeding a particular level x. Overall, approach 2 (Mazas et al.) and approach 3 (Tawn and Vassie) performed more or less equally well. However, as approach 3 has a better theoretical underpinning when extrapolating beyond the range of observations, this is our preferred approach. The complete marginal distribution function, described by Eq. (19) for each residual current component X_i, is thus calculated with $\theta_{x_i}^{-1}(x)$ as determined by *approach 3*.

As an anecdote to the above discussion, it is worth mentioning that we performed the dependence modelling and the conditional simulations described in the following subsections using all the three approaches described above for estimation of $\theta_x^{-1}(x)$. Somewhat surprisingly, at both considered locations, only small differences were observed in the resulting predicted extreme current velocity profiles. This seems to suggest that, provided the same approach is used to estimate $\theta_{x_i}^{-1}(x)$ for all X_i, accurate estimation of the extremal index is not the most critical step in the current statistical model.

5.3. Dependence modelling

We now turn to the modelling of the extremal dependence between the residual current velocity components. Most of the details have already been described in Section 4, however, some modifications to the original model (Heffernan and Tawn, 2004) are needed to allow modelling of 'instantaneously' observed mean current velocity profiles.

The conditional extremes model by Heffernan and Tawn concerns the estimation of functionals of the conditional distribution of $\mathbf{X}_{-i} | X_i > v_{X_i}$. As originally formulated, each observation of $\mathbf{X}$ is assumed to be independent and with no components of $\mathbf{X}$ missing. Both these assumptions are violated for our data, calling for an extension of the original model. Solutions to similar problems were given by Keef et al. (2009), however, due to differences in the involved variables, the proposed methods are unfortunately not applicable to our data. More specifically, the issues which needs to be addressed are:

1. The hourly recorded current velocity profiles displays temporal dependence, requiring a condition to be introduced to limit the effect of dependence. Owing to the multidimensionality of the problem, it is however difficult to introduce a very strict condition to reduce dependence (as the observed individual residual current components do not necessarily peak at the same

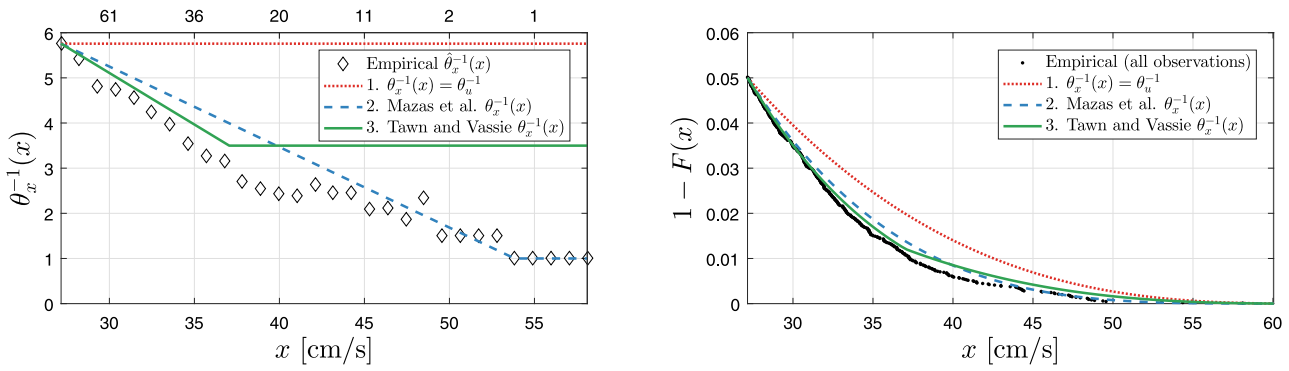

Fig. 12. (a) Estimated inverse extremal index $\theta_x^{-1}(x)$ by the three considered approaches plotted against the empirical estimates $\hat{\theta}_x^{-1}(x)$ for residual current component u_{RM}^{+} at 4 m depth at Munkskjæra. The number of cluster maxima above each labelled level x is indicated on the upper axis. (b) The resulting survival function $\bar{F}(x) = 1 - F(x)$ plotted against the empirical 'all observation' estimates in the upper tail $x \geq u$.

time during an event with strong consecutive currents, it is, as opposed to for univariate peaks over threshold modelling, difficult to decide which of the observed current profiles that should be considered as the 'peak' observation).

2. The d-dimensional vector of simultaneously observations $\mathbf{X}$ includes $d/2$ observed and $d/2$ unobserved residual current components. This is not an issue of missing values due to measurement malfunction, but simply a consequence of how the current components are defined (cf. Section 5.1).

The dependence model is applied to the data after transformation to Laplace margins. The original vector variable $\mathbf{X}$ with marginal distributions defined by Eq. (19), is thus transformed componentwise by transformation (5) to a vector variable $\mathbf{Y}$ with Laplace distributed marginals.

Point 1 above is taken care of marginally by application of the peaks over threshold method in the same way as when fitting the marginal tail distributions in Section 5.2.2. This means that the semiparametric regression model (10), which for large Y_i describes the behaviour of the remaining components in $\mathbf{Y}$, is only fitted to observations of $\mathbf{Y}|Y_i > u_{Y_i}$ where Y_i corresponds to a *cluster peak excess*. For each conditioning variate Y_i, $i = 1, \ldots, d$, of independent cluster peak excesses, the resulting observations $\mathbf{Y}|Y_i$ can then also be considered independent. The minimum peak-to-peak separation time τ_{Y_i} is set equal to the marginal minimum peak-to-peak separation time τ_{X_i} (here, 30 h). The dependence thresholds u_{Y_i}, which does not need to equal the marginal thresholds u_{X_i} in the sense that $F_{Y_i}(u_{Y_i}) = F_{X_i}(u_{X_i})$, can be decided based on assessing the stability of the estimates of $(\boldsymbol{\alpha}_{|i}, \boldsymbol{\beta}_{|i})$ for a range of thresholds and examining the independence of $\mathbf{Z}_{|i}$ and Y_i (see Heffernan and Tawn (2004) for further details regarding diagnostics).

Point 2 constitutes an issue for structure and consistency in the system of equations and for the construction of, and simulation from, the distribution function $G_{|i}$. Consistency in the system of equations can be obtained by careful vector treatment, ensuring that the conditional model (10) is fitted only to the components $Y_{j|i}$ of $\mathbf{Y}_{-i}$ which were observed simultaneously as Y_i. In the construction of $G_{|i}(\mathbf{z}_{|i})$ we take advantage of the lack of imposed structure on $G_{|i}$ in Heffernan and Tawn (2004) and the (false) assumption that the components of $\mathbf{Z}_{|i}$ are mutually independent and Gaussian distributed during inference. The independence assumption renders possible componentwise estimation of the vector constants in Eq. (10). This makes it easier to allow for a few difficulties that arises because of how the residual current components making up $\mathbf{Y}$ are defined (Eq. (13)).

Specifically, for a given conditioning variate Y_i corresponding to a cluster peak excess, there are certain restrictions on which components in $\mathbf{Y}_{-i}$ that can be observed simultaneously as Y_i. For instance, if Y_i corresponds to a positive major axis velocity component at a particular depth, it is not possible to simultaneously observe a negative major axis velocity component at the same depth and vice versa. Also, due to spatial dependence, there will generally be other combinations of $(Y_i, Y_{j|i})$, $j \neq i$, that are highly unlikely to occur together — physically, it is quite intuitive that given an extreme current velocity in a particular direction at one depth, the current would be expected to flow in approximately the same direction at adjacent depths. The practical consequence of this is that for some $Y_{j|i}$ we have no, or very few, observations to estimate the corresponding dependence parameters $(\alpha_{j|i}, \beta_{j|i})$. For the $Y_{j|i}$ with no observations this is not an issue; $G_{|i}$ is modelled by its empirical distribution function, so for a given Y_i, such Y_j will have zero probability of occurrence, making dependence modelling redundant. For the $Y_{j|i}$ with just a few observations, estimates of $(\alpha_{j|i}, \beta_{j|i})$ will be unreliable due to the small sample size. After careful inspection of the data at the two considered locations, it was found that such $Y_{j|i}$ always corresponded to velocity components in the opposite direction[2] of Y_i at adjacent depths. Physical considerations suggests that these pairs (Y_i, Y_j) are negatively dependent. Denoting the number of observations of $Y_{j|i}$ by $n_{Y_{j|i}}$, we therefore set $(\alpha_{j|i}, \beta_{j|i}) = (-1, 0)$, corresponding to negative asymptotic dependence, for all $Y_{j|i}$ with just a few observations.[3] For the data at hand we defined 'a few' as $n_{Y_{j|i}} \leq 12$.

The remaining $\alpha_{j|i}$ and $\beta_{j|i}$ (and nuisance parameters $\mu_{j|i}$ and $s_{j|i}$) are estimated by numerical minimization of the negative of the components $Q_{j|i}$ of the objective function (11) over the parameter space of the model, only summing over the $y_{i|i}$ and $y_{j|i}$ observed simultaneously. For both computational efficiency and stability, it was found favourable to first perform the minimization without imposing the constraints in Keef et al. (2013), and then, using the resulting estimates as a starting point, run the minimization again with the additional constraints in Keef et al. (2013). The constraints were imposed on $y_i > v$, where for each Y_i, v was taken equal to the estimated marginal 50-year return level of Y_i. As found in Keef et al. (2013), the results showed little sensitivity to the precise choice of v as long as v was taken above the maximum observed value of Y_i.

Based on the point estimates $(\hat{\boldsymbol{\alpha}}_{|i}, \hat{\boldsymbol{\beta}}_{|i})$, the observations $\hat{\mathbf{z}}_{|i}$ of the random normalized residual $\mathbf{Z}_{|i}$ are given by Eq. (12). The number of observations of $\hat{\mathbf{z}}_{|i}$ is equal to the number of cluster peak excesses of Y_i, denoted n_{Y_i}, and provide a sample from $G_{|i}$. Since each $\mathbf{Y}_{-i}$ formally contains $(d/2 - 1)$ observed and $d/2$ unobserved components, so will $\hat{\mathbf{z}}_{|i}$. The dependence between the components, partly in terms

[2] If, for instance, Y_i corresponds to a positive major axis component, we mean by 'opposite direction', $Y_{j|i}$ corresponding to negative major axis components.

[3] If found to be unimportant for extremes, an alternative can be to simply neglect/ignore these observations.

of magnitude, but more importantly in terms of which components are simultaneously observed and which are unobserved, is taken care of by modelling $G_{|i}$ by its empirical distribution function $\hat{G}_{|i}$. The probability of observing a given component $Z_{j|i}$ from $\hat{G}_{|i}$ is equal to $n_{Y_{j|i}}/n_{Y_i}$. When sampling from $\hat{G}_{|i}$ in the subsequent conditional simulation, the number of observed $Z_{j|i}$ (and $Y_{j|i}$) will thus follow a binomial distribution.

By conditioning on the cluster peak excesses of each of the d variates in turn, the dependence model was estimated. As in Jonathan et al. (2012), and for many of the parameters examined in Heffernan and Tawn (2004), it was found that conditional thresholds equalling the marginal thresholds (in terms of quantiles) gave reasonable stable results. A dependence threshold equivalent to the 95% quantile for Y_i corresponding to major axis components and the 94% quantile for Y_i corresponding to minor axis components was thus selected.

The resulting estimates of the dependence parameters $\alpha_{j|i}$ and $\beta_{j|i}$ when conditioning on Y_1 and Y_3 at Munkskjæra, are shown in Fig. 13, including the effect of imposing the Keef et al. (2013) constraints. For conditioning variate Y_1, corresponding to the major axis velocity component $u^+_{RM,1}$, strong dependence is seen with u^+_{RM} at all other depths. Weaker dependence is seen with minor axis components. There are no observations of simultaneously reversing currents at other depths (u^-_{RM}) except one low-velocity observation (< 1cm/s) at depth number 3 (16 m), indicated by the single black dot with $(\alpha_{|1}, \beta_{|1}) = (-1, 0)$ in Fig. 13(a). For conditioning variate Y_3, corresponding to the minor axis component $u^+_{Rm,1}$, strong dependence is seen for other u^+_{Rm}, getting weaker with depth. Only weak dependence with other components is seen. Current reversals occur relatively frequent from depths 3–6 (u^-_{Rm}), the frequency increasing with depth. Qualitatively similar results as in Fig. 13 were observed when conditioning on other major and minor axis components at Munkskjæra.

It is noticeable that the estimated dependence parameters are generally smoother with depth for velocity components with strong dependence (e.g. for u^+_{RM} in Fig. 13(a)) than for those with weak dependence. As the estimated parameters are expected to vary relatively smoothly with depth, this indicates that it can be more challenging to accurately estimate the dependence parameters for velocity components with weak association. In addition, the estimated α are usually smoother than those for β; Jonathan et al. (2010, 2014) notes that there are some redundancy between β and the nuisance parameters μ and s, which can probably help explain this. As a consequence, it is observed that the non-smooth parameter estimates are, to some extent, compensated by the residuals $Z_{j|i}$ in the conditional simulation, yielding smoother simulated current profiles.

An illustration of the fitting of the dependence model (10) by log-likelihood (11) is shown in Fig. 14. Simultaneous observations of Y_{13}, corresponding to $u^+_{RM,4}$, and cluster peak excesses of conditioning variate Y_1, corresponding to $u^+_{RM,1}$, are displayed together with the fitted mean and standard deviation of Y_{13} as a function of Y_1. The estimated near asymptotic dependence between these two variables, as indicated in Fig. 13(a), is seen to be well supported by the data. In Fig. 14(b), the resulting normalized residuals $\hat{z}_{13|1}$ plotted against Y_1 are shown. Such plots, where the independence of $Z_{j|i}$ and Y_i is examined (independence is a modelling assumption), are part of the diagnostics to assess model fit. No obvious dependence between $Z_{13|1}$ and Y_1 is seen.

5.4. Conditional simulation

As previously mentioned, estimates of various extremal statistics must be acquired by simulation. The simulation is performed using the Monte Carlo sampling algorithm described in Section 4.4. To account for temporal dependence, a slight modification of how to determine the number of times which to condition on each variable has to be made compared to that proposed by Jonathan et al. (2012). Following the methodology from the marginal and dependence modelling, we consider only the marginal cluster peak excesses of each X_i, $i = 1, \ldots, d$.

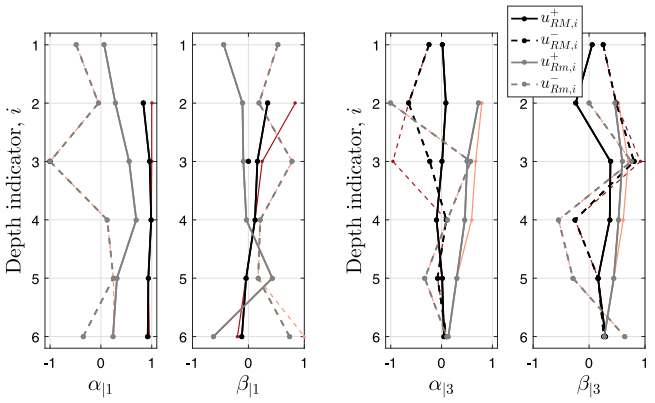

(a) Conditional on Y_1 ($u^+_{RM,1}$). (b) Conditional on Y_3 ($u^+_{Rm,1}$).

Fig. 13. Estimated dependence parameters $\alpha_{j|i}$ and $\beta_{j|i}$ when conditioning on (a) Y_1, corresponding to $u^+_{RM,1}$, and (b) Y_3, corresponding to $u^+_{Rm,1}$, at Munkskjæra. Red lines show the estimated dependence parameters *without* imposing the constraints in Keef et al. (2013); darker red lines correspond major axis components and lighter red lines to minor axis components. (For interpretation of the references to colour in this figure legend, the reader is referred to the web version of this article.)

Transformed to Laplace distributed variables Y_i, the *yearly* number of times which to condition on each Y_i is then determined by the number of times which Y_i is the only or the largest simultaneously observed Y corresponding to a cluster peak excess, divided by the effective number of years of observations. We thus ensure that the number of simulated current profiles per year is equal to the average number of yearly observed residual current profiles with at least one velocity component corresponding to a (marginal) cluster peak excess.

When performing the conditional simulation, a critical point has to be made clear in order to ensure consistency regarding how to determine which components of the simulated $\mathbf{Y}_{-i}$ that should be observed and which should not. The key point is that subsequent to having simulated a value of the conditioning variate Y_i, we sample $\mathbf{Z}_{|i}$ by randomly drawing (with replacement) one of the n_{Y_i} observed vectors $\hat{\mathbf{z}}_{|i}$ making up $\hat{G}_{|i}$. The $(d/2 - 1)$ observed components of the drawn $\hat{\mathbf{z}}_{|i}$ then determines which components of the simulated vector $\mathbf{Y}_{-i}$, obtained by Eq. (10), that are observed and which are not. In that way, the (generally strong) dependence between the components in terms of which are simultaneously observed are taken care of. Physically, this ensures that the directional misalignment of the current velocity at different depths for a simulated current profile is approximately within the range observed in the measurements. The components of $\hat{\mathbf{Z}}_{|i}$ can thus *not* be modelled as being independent (i.e. $\hat{G}_{|i}(\mathbf{z}_{|i}) \neq \prod_{j \neq i} \hat{G}_{j|i}(z_{j|i})$). A simplification involved using this approach is that the probability of observing a particular $Y_{j|i}$ does not depend on the magnitude of the simulated value of Y_i. Though quite laborious, it would be possible to also model such dependence, but as long as the conditional threshold is set sufficiently high, it does not appear to affect the results in any critical way.

A simulated total current profile is obtained by adding a simulated residual current profile and a predicted tidal current profile, assuming the residual and tidal current to be independent. Since the tidal current for practical purposes can be considered as periodic with period 18.6 years (the nodal cycle), predicting hourly tidal current profiles over this period is sufficient to fully describe the distribution of the tidal current profiles. The predictions are made by the harmonic analysis described in Section 3.2, and the tidal current profiles are drawn at random from the resulting sample of size 18.6×8766 (the number of hourly observations during 18.6 years).

Having decided the yearly number of times which to condition on each Y_i, $i = 1, \ldots, d$, the full sampling algorithm for each Y_i for simulating total current velocity profiles over a desired period is as follows:

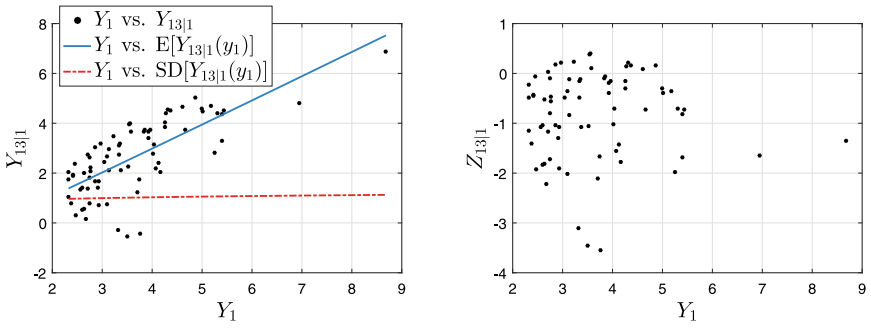

(a) Model fitting of $Y_{13|1}$. (b) Normalized residuals $\hat{z}_{13|1}$.

Fig. 14. (a) Fitting of the dependence model to simultaneous observations of Y_{13}, corresponding to $u^+_{RM,4}$ and cluster peak excesses of conditioning variate Y_1, corresponding to $u^+_{RM,1}$. $\mathrm{E}[Y_{13|1}(y_1)] = \alpha_{13|1} y_1 + \mu_{13|1} y_1^{\beta_{13|1}}$ is the fitted mean value of $Y_{13|1}$ and $\mathrm{SD}[Y_{13|1}(y_1)] = s_{13|1} y_1^{\beta_{13|1}}$ is the standard deviation. (b) The resulting normalized random residuals $\hat{z}_{13|1}$ displays no obvious dependence with Y_1.

1. Simulate a cluster peak excess of X_i ($> u_{X_i}$) from the generalized Pareto distribution, Eq. (15). Transformation (5) (via Eq. (19)) yields a simulated Y_i.
2. Sample $\mathbf{Z}_{|i}$ by drawing (with replacement) one of the n_{Y_i} observed vectors $\hat{\mathbf{z}}_{|i}$.
3. Obtain $\mathbf{Y}_{-i} = \hat{\boldsymbol{\alpha}}_{|i} Y_i + Y_i^{\hat{\boldsymbol{\beta}}_{|i}} \hat{\mathbf{z}}_{|i}$. The $(d/2 - 1)$ observed components of $\hat{\mathbf{z}}_{|i}$ determines which components of $\mathbf{Y}_{-i}$ that are observed and which are not.
4. Transform $\mathbf{Y} = (\mathbf{Y}_{-i}, Y_i)$ to $\mathbf{X}$ using the inverse of transformation (5) to obtain a simulated residual current velocity profile.
5. Draw (with replacement) a tidal current velocity profile from the sample of 18.6 years of predicted tidal current profiles.
6. Add the realizations of residual and tidal current profiles to obtain a simulated total current velocity profile.

Due to the introduction of an extremal index varying with level x in Eq. (19), the inverse of transformation (5) in step 4 above, used to transform $\mathbf{Y}$ to the original scale $\mathbf{X}$, cannot always be solved analytically. To avoid the use of time-consuming numerical solvers in the simulation procedure, it is favourable to, in advance, fit a higher order polynomial to describe the relationship between X_i and Y_i on the range $u_{X_i} \leq x \leq x_{lim,i}$ (the range for which $\theta_{x_i}^{-1}(x)$ is not a constant).

If interest is in submodels, obvious modifications to the simulation procedure must be made.

5.5. Simulated current profiles

With the estimated marginal and conditional extremes models, arbitrary long time series of extreme current velocity profiles can be simulated by the sampling algorithm described in Section 5.4. To illustrate some results, we have simulated 1000 years of extreme current profiles at both Munkskjæra and Salatskjæra.[4] Particular focus will be placed on the residual current profiles as it is only the residual current that is described by the conditional extremes model.

In Fig. 15 and 16, the resulting simulated median marginal 10-year return values for all four residual current components at each depth are illustrated for Munkskjæra and Salatskjæra, respectively. The median 10-year return values and the quantile intervals are found by splitting the 1000 years of simulated residual current profiles into 10-year periods, extracting componentwise maxima, fitting a generalized extreme value (GEV) distribution to the resulting 100 block maxima for each variable, and extracting the 2.5%, 50% and 97.5% quantiles from the GEV distributions.[5] For comparison and partial validation of

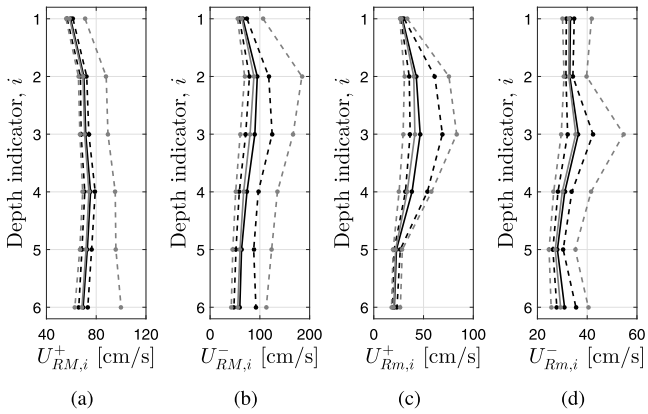

Fig. 15. Median marginal 10-year return values for all residual current components at Munkskjæra estimated from the conditional simulation (solid black) and from the fitted marginal models (solid grey). Dashed black lines are 2.5% and 97.5% quantiles from the simulations, dashed grey lines are 95% confidence intervals based on profile likelihood from the fitted marginal models.

the dependence modelling and simulation procedure, the median 10-year return values and corresponding 95% profile likelihood confidence intervals calculated from the fitted marginals from Section 5.2 are also shown (note that the calculated median 10-year return values from the fitted marginals are not equal to the 10-year return values estimated by Eq. (16) as the latter correspond to $\approx 37\%$ quantiles). The simulated median return values are seen to closely follow those calculated from the fitted marginals; the simulated values consistently being slightly higher. The tendency of a small positive bias is primarily related to the choice of only accounting for temporal dependence marginally when determining the number of current profiles to be simulated per year. Though, compared to the confidence intervals of the fitted marginals, the difference is generally negligible. The tighter confidence intervals from the simulations are a natural consequence of the parametric bootstrap procedure used to obtain them.

Emphasizing the stochastic nature of the plots, simulated and observed residual, tidal and total current velocities at 4 m depth at both Munkskjæra and Salatskjæra are illustrated in Fig. 17 (note that the velocities have been transformed back to eastward and northward components). Only the first 10-year period of the simulated velocities are shown. To resemble the simulated velocities, only observations from the measurements where at least one of the residual current components of the velocity profile corresponds to a marginal cluster peak excess, are plotted. The simulated residual current velocities, based on the conditional extremes model, are seen to closely follow the trends of the observations. Looking at the simulated total currents,

[4] The single-core computational time was between 15 and 20 min on an Intel i7 (3 GHz) processor for each location.

[5] Simple empirical quantile estimates gave almost identical results.

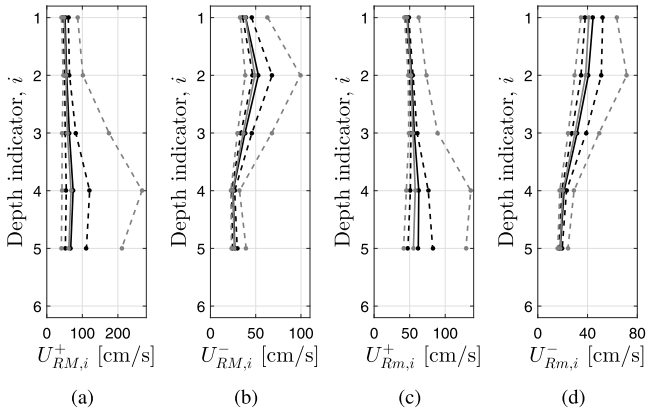

Fig. 16. Median marginal 10-year return values for all residual current components at Salatskjæra estimated from the conditional simulation (solid black) and from the fitted marginal models (solid grey). Dashed black lines are 2.5% and 97.5% quantiles from the simulations, dashed grey lines are 95% confidence intervals based on profile likelihood from the fitted marginal models.

they are also seen to match the observed total currents quite well, particularly at Munkskjæra. At Salatskjæra (Fig. 17(f)), there are apparent evidence of some interaction between the tidal and the residual current; the main effect being suppression of total current velocities in the northeastern direction. Similar interaction (though less pronounced) is apparent in the eastward direction at Munkskjæra. Such interactions are not captured by the statistical model as independence between the tidal and the residual current is an inherent assumption. However, when including all observations from the measurements in the plot (not shown), the interaction is less pronounced at Salatskjæra. In the context of extreme value analysis, it is reassuring that the most extreme simulated total current velocities, both in terms of magnitude and direction, coincide reasonably well with those from the observations. Similar agreement between simulated and observed velocities are seen at all other considered depths.

So far, only marginal and single-depth results have been presented. In isolation, these results are of limited interest as our main objective is to characterize instantaneous extreme current velocity *profiles* with depth. Presenting such multivariate data in a visually appealing manner is however challenging, and we therefore present the instantaneous current profile results in terms of integrated variables. Since we are usually interested in the resulting force vector due to the current velocity profile for design of coastal and ocean structures, such a measure is considered to be the most informal two-dimensional summary of the current velocity profiles.

Let us consider the resulting force on a fixed, surface piercing, vertical circular cylinder with diameter $D = 1$ m and submerged length h. The length h is taken equal to 35 m for Munkskjæra and 30 m for Salatskjæra, so that the bottom of the cylinder is at a depth slightly lower than the deepest measurement point at the respective locations (34 m and 28 m). The resulting Cartesian force components, or loads, L_e and L_n in the eastward and northward direction, respectively, are given by the quadratic drag equation, which for a vertical cylinder exposed to a horizontal current takes the form

$$\begin{aligned} L_e &= \tfrac{1}{2}\rho C_d D \int_{-h}^{0} u_e(z)\sqrt{u_e(z)^2 + u_n(z)^2}\,\mathrm{d}z \\ L_n &= \tfrac{1}{2}\rho C_d D \int_{-h}^{0} u_n(z)\sqrt{u_e(z)^2 + u_n(z)^2}\,\mathrm{d}z \end{aligned} \tag{22}$$

where we take the water density $\rho = 1000$ kg/m^3 and the drag coefficient $C_d = 1$. The eastward and northward velocities u_e and u_n are functions of the vertical coordinate z ($z = 0$ at the sea surface). A two-dimensional illustration is shown in Fig. 20. For all observed and simulated current velocity profiles, Eq. (22) is solved by numerical integration over the length of the cylinder, assuming a linear velocity profile between the discrete measurement points (and a constant velocity above the highest and below the lowest measurement point). By applying bivariate kernel density estimation (see, e.g., Silverman (1986)), a smooth, empirical estimate of the joint probability density function $f_{L_eL_n}(l_e, l_n)$ can be obtained. The resulting joint probability densities are then transformed to polar coordinates (force magnitude L and direction Φ). The conditional cumulative distribution function of force given direction, $F_{L|\Phi}(l|\phi)$, can then be estimated, allowing for estimation of extreme quantiles of the resulting force given direction.

In Fig. 18, estimates of the 0.95, 0.99 and 0.995 quantiles of the conditional distribution of force given direction due to the residual current and total current velocity profiles at Munkskjæra are presented, both from the simulations and the observations. The observation samples are also plotted (again, only observations where at least one of the residual current components of the velocity profile corresponds to a cluster peak excess are considered). Fig. 19 displays a similar plot for Salatskjæra. At both sites, the quantiles of the forces from the simulated current profiles are seen to follow the trends of the observations well — particularly the residual current forces. The estimates of the 0.95 quantile residual current forces are very similar, as is expected. Due to the limited sample size, the higher quantiles estimated from the observations are expected to be poorly estimated empirically, and are dominated by outlying data and the choice of kernel bandwidth parameter — however, in terms of both magnitude and direction, the observed and simulated quantiles are still in reasonable agreement. The slightly 'rough' quantile curves from the simulations are a consequence of the semiparametric nature of the conditional extremes model (though, smoother estimates can obviously be obtained by increasing the kernel bandwidth). The additional discrepancies for the total current forces compared to the residual current forces alone, are primarily related to the increased variability (randomness) introduced when combining residual and tidal current profiles and residual–tidal current interaction. At Munkskjæra (Fig. 18(b)), there are some evidence of interaction between the tidal and residual current in the eastward direction, making the independence assumption appear slightly conservative. At Salatskjæra (Fig. 19(b)), similar effects are seen in the northeastern direction, in addition to an apparent clustering of extreme total current forces in the eastward direction (both these effects can be also be seen in Fig. 17(f)). Notwithstanding these effects, the simulated total current forces are generally in reasonable agreement with those from the measurements.

As it has already been demonstrated that the simulated current velocity components are consistent, both marginally and jointly at each depth, the agreement between simulated and observed resulting forces suggests that the simulated current velocity *profiles* are also consistent.

6. Design current velocity profiles

From a structural design perspective, the key output from a statistical analysis of current profiles is so-called *design current velocity profiles*. In principle, such design profiles should not be estimated in isolation of other relevant environmental parameters. However, as the focus of this paper is on current velocity profiles only, we do not consider the additional effect of other environmental phenomena (such as waves and wind) when deciding these. Reference is made to offshore standards and recommended practices such as ISO (2015) and DNV (2014) for important joint environmental and structure-specific considerations. An example of a pragmatic way of accounting for the effect of the additional wave-induced fluid velocity, is found in Winterstein et al. (2011), resulting in increased importance (weighting) of near-surface currents.

When designing coastal or ocean structures, design values of important metocean parameters are required to ensure that the structure in question can withstand the extreme environmental conditions expected to occur at the location(s) where it is to be operated. The required design values are usually specified in terms of return periods or annual

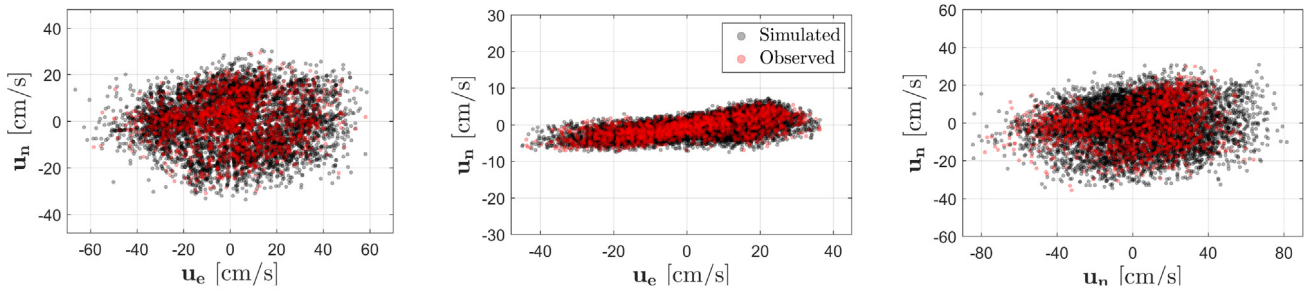

(a) Residual current at 4 m, Munkskjæra. (b) Tidal current at 4 m, Munkskjæra. (c) Total current at 4 m, Munkskjæra.

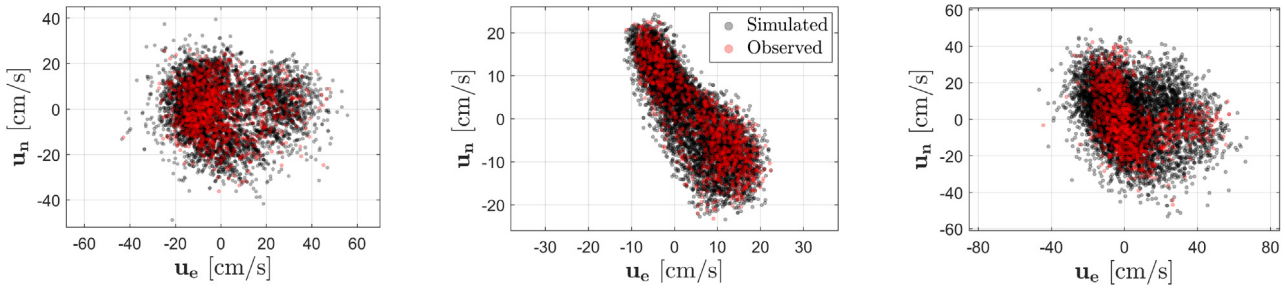

(d) Residual current at 4m, Salatskjæra. (e) Tidal current at 4 m, Salatskjæra. (f) Total current at 4 m, Salatskjæra.

Fig. 17. 10 years of simulated (grey) residual, tidal, and resulting total current velocities at 4 m depth at Munkskjæra (upper) and Salatskjæra (lower) compared to the observations (red). Only observations where at least one of the residual current components of the velocity profile corresponds to a marginal cluster peak excess are plotted. The stochastic nature of the residual and total current velocity plots is emphasized.

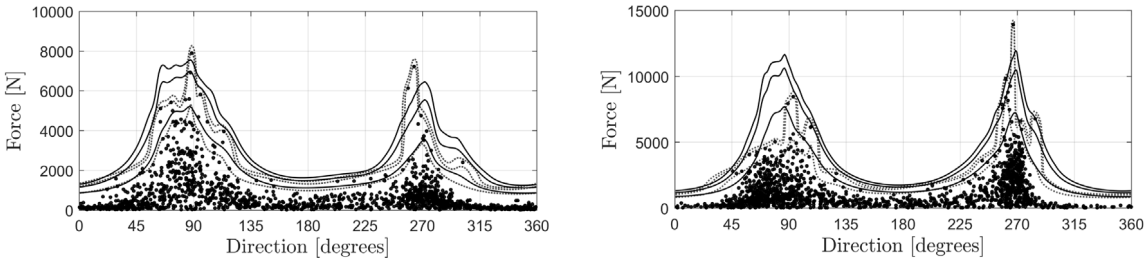

(a) Residual current force, Munkskjæra. (b) Total current force, Munkskjæra.

Fig. 18. 0.95, 0.99 and 0.995 quantiles of the conditional distribution of radial resulting force given direction for residual and total current profiles at Munkskjæra: (——) simulations; (·····) observations. The black dots show the sample which the observation quantiles are based on, and correspond to the resulting force from the observations where at least one residual current component of the velocity profile is a marginal cluster peak excess. The direction is measured clockwise from north.

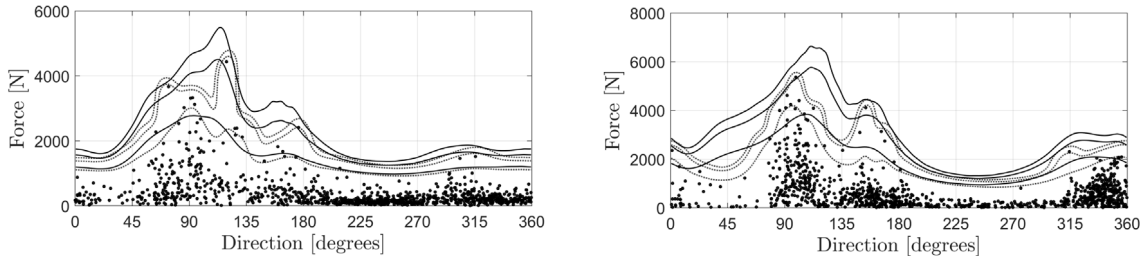

(a) Residual current force, Salatskjæra. (b) Total current force, Salatskjæra.

Fig. 19. 0.95, 0.99 and 0.995 quantiles of the conditional distribution of radial resulting force given direction for residual and total current profiles at Salatskjæra: (——) simulations; (·····) observations. The black dots show the sample which the observation quantiles are based on, and correspond to the resulting force from the observations where at least one residual current component of the velocity profile is a marginal cluster peak excess. The direction is measured clockwise from north.

probabilities of occurrence (the reciprocal of the return period). For a univariate metocean parameter, the value corresponding to a given return period is uniquely defined once its marginal distribution has been established. In the case of multivariate metocean data – like current velocity profiles – this is not so, however, and some sort of sub-ordering principle (see Barnett (1976) for an overview) is useful to employ for easier identification of multivariate (extreme) design values. In the context of structural design, sub-ordering of multivariate environmental phenomena is usually achieved through a generic load model that effectively combines the environmental variables into a relevant response (Tromans and Vanderschuren, 1995).

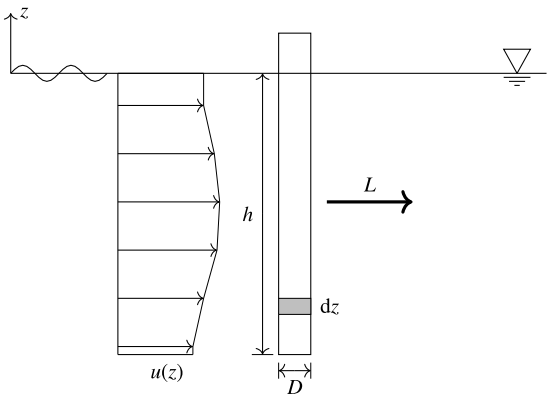

Fig. 20. Two-dimensional illustration of the resulting force, L, due to a current velocity profile, $u(z)$, acting on a vertical circular cylinder. The arrows of the profile indicate the considered depths at the Munkskjæra site with $h = 35$ m.

The resulting total drag force on the structure in question is among the most informal summary variables of the effect of the current velocity profiles on a wide range of marine structures. Since the current can usually be considered as a steady flow field where the velocity vector is only a function of depth (ISO, 2015; DNV, 2014), this force can usually be calculated without much effort — at least within the degree of accuracy required here. The first step in our approach for deciding design current velocity profiles therefore involves calculating the total drag force (or another relevant response function) due to the simulated current velocity profiles. We outline the approach below by considering a simple example. It should however be mentioned that, due to the flexibility of the conditional extremes model, a range of alternative strategies will also be applicable besides the one presented here.

6.1. Example — Design current velocity profiles on a vertical circular cylinder

Following the example in Section 5.5, we consider the total drag force vector due to the current velocity profiles, acting on a vertical circular cylinder with diameter $D = 1$ m and submerged length h; see Fig. 20 for a two-dimensional illustration. Again, h is taken equal to 35 m for Munkskjæra and 30 m for Salatskjæra. This is a simplified, but representative example of a floating (moored) structure exposed to currents. For all the simulated 'extreme' total current velocity profiles, covering the 1000 year simulation period, the Cartesian total drag force components are obtained by solving Eq. (22) by numerical integration over the length of the cylinder. At the Munkskjæra site, this means calculating the resulting force due to approximately 755000 current profiles (on a state-of-the-art laptop, this required only a few minutes of CPU time when using a discrete step size $\mathrm{d}z = 1$ m in the numerical integration). The Cartesian force components are conveniently transformed to polar coordinates, yielding force magnitudes, L, and associated directions, $\boldsymbol{\Phi}$.

By looking at the resulting response (the total drag force vector) instead of the current velocity profiles directly, our multivariate problem has effectively been reduced to a two-dimensional one.[6] N-year design current velocity profiles can then be obtained by first estimating the N-year drag force (favourably as a function of direction) and subsequently deriving corresponding current velocity profiles, yielding an equivalent force.

[6] The entire extreme value analysis could indeed have been performed on the structural response/load directly (as opposed to the current profiles), but this would have left us with little knowledge about the actual shape of the current velocity profiles causing the extreme responses.

6.1.1. Estimating design drag forces

Robinson and Tawn (1997) describe various ways of estimating design values of a two-dimensional vector variable (with a magnitude and a direction). Applying these methods, both omni-directional and directional return values of the (simulated) drag forces can be obtained. Two aspects greatly simplifying this step are; (1) since temporal dependence has already been (partly) accounted for in the Monte Carlo sampling algorithm, the simulated drag forces can be considered as independent; (2) provided the simulation period is substantially longer than the return periods of interest (say, *at least* 10–20 times longer), return values can be estimated directly from the simulated sample without the need of first fitting a parametric probability distribution.

Denoting the yearly number of simulated current velocity profiles $n_{S,1y}$, the estimated omni-directional N-year return value of the drag force, l_N, is obtained by solving for the load that satisfies

$$F_L(l_N) = 1 - \frac{1}{n_{S,1y} N} \tag{23}$$

As we only consider return periods, N, that are substantially shorter than the simulation period, the distribution function of the drag load, $F_L(l)$, can conveniently be approximated by its empirical distribution function.

Directional return values can be obtained by looking at the probability that the drag load is exceeded in a particular direction, providing information on the required directional structural strength. Following the discussion in Robinson and Tawn (1997), each simulated observation of $(L, \boldsymbol{\Phi})$ has a resolved drag load in every non-orthogonal direction; i.e. the observation (l, ϕ) has a resolved load $l(\psi) = l\cos(\phi - \psi)$ in each direction $\psi \in (0, 2\pi]$. For regularly spaced directions ψ_j, the resolved load $l(\psi_j)$ can be calculated for all the simulated observations $(L, \boldsymbol{\Phi})$. The N-year return value, $l_N(\psi_j)$, for the resolved loads in direction ψ_j, are then calculated by solving

$$F\left(l_N(\psi_j)\right) = 1 - \frac{1}{n_{S,1y} N} \tag{24}$$

with $F\left(l(\psi_j)\right)$ approximated by its empirical distribution function.

Instead of resolved loads, one might be interested in the load $l^*_N(\psi_\delta)$ which is exceeded, on average, once every N years, conditional on the direction being in sector ψ_δ; ψ_δ being a sector of width δ centred on $\phi = \psi$. Such estimates will depend on the sector width δ, which should be decided taking both the structure and the directional variation of the load into consideration. Note that the sectors do not need to be equal in size, but for design, ISO 19901–1 recommends that the sector width should not be smaller than 45° to avoid 'over-optimization' (ISO, 2015). To decide $l^*_N(\psi_\delta)$, the conditional distribution of $l^*(\psi_\delta)$ given ψ_δ is required, i.e.

$$F\left(l^*(\psi_\delta) \mid \psi_\delta\right) = \int_0^{l^*(\psi_\delta)} \int_{\psi-\delta/2}^{\psi+\delta/2} f_{R,\boldsymbol{\Phi}}(r, \phi)\, \mathrm{d}\phi\, \mathrm{d}r / p_{\psi_\delta} \tag{25}$$

where p_{ψ_δ} is the probability of being in sector ψ_δ. Both p_{ψ_δ} and $F\left(l^*(\psi_\delta)|\psi_\delta\right)$ can be estimated empirically. Particularly for small δ, a bivariate kernel density estimate of $f_{R,\boldsymbol{\Phi}}(r, \phi)$ can provide smoother directional estimates. Finally, the return level $l^*_N(\psi_\delta)$ can be estimated by solving

$$F\left(l^*_N(\psi_\delta)|\psi_\delta\right) = 1 - \frac{1}{n_{S,1y} N p_{\psi_\delta}} \tag{26}$$

Applying the three approaches described above, Figs. 21 and 22 shows estimates of extreme drag forces corresponding to return periods $N = 10$, 50 and 100 years at Munkskjæra and Salatskjæra, respectively. At Munkskjæra, the critical directions are clearly bounded to the east and west. Looking at the resolved force estimates, $l_N(\psi)$, we note that the 10-year force is approximately of equal magnitude in the eastward and westward direction, however, for increasing N, the difference magnifies, reflecting the long tail (higher GP shape parameter) of the westward flowing current components; cf. Fig. 10(a). At Salatskjæra, the critical direction is in a quite wide sector to the southeast. An

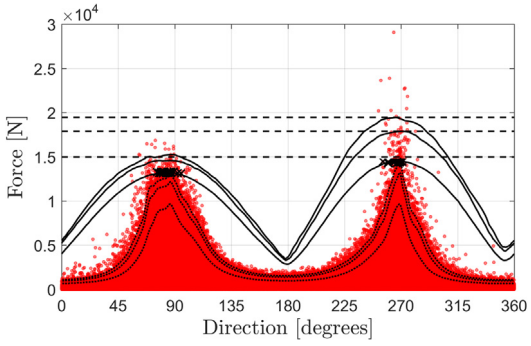

Fig. 21. Munkskjæra: N-year return value force estimates due to the simulated current velocity profiles for $N = 10$, 50 and 100 years. (– – –) omni-directional force l_N; (——) resolved forces $l_N(\psi)$; (· · · · ·) forces conditional on direction $l^*_N(\psi_\delta)$. The red dots show the simulated 1000 year sample which the estimated return values are based on. Black crosses are the two samples which the 10-year design profiles in Fig. 23 are based on.

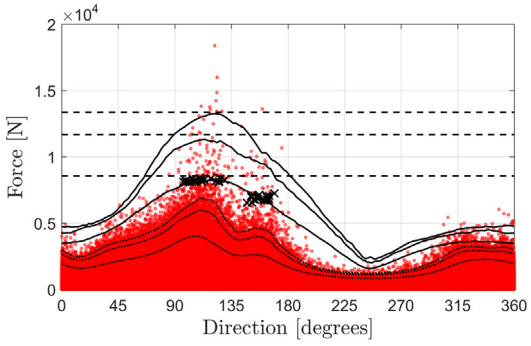

Fig. 22. Salatskjæra: N-year return value force estimates due to the simulated current velocity profiles for $N = 10$, 50 and 100 years. (– – –) omni-directional force l_N; (——) resolved forces $l_N(\psi)$; (· · · · ·) forces conditional on direction $l^*_N(\psi_\delta)$. The red dots show the simulated 1000 year sample which the estimated return values are based on. Black crosses are the two samples which the 10-year design profiles in Fig. 24 are based on.

interesting feature is the local force-minima at approximately 135°, seen for the conditional force estimates, $l^*_N(\psi_\delta)$. This local minima is also apparent in the measurements (Fig. 19(b)), and is probably related to the presence of a few small islands and skerries upstream for flow in this direction. It is pleasing to observe that the proposed statistical model is able to capture such complex directional behaviour.

The estimates of $l^*_N(\psi_\delta)$ (force conditional on direction) have similar directional characteristics as those of the resolved forces $l_N(\psi)$, but are smaller in magnitude because large forces in other directions can have resolved forces which exceed observed forces in direction sector ϕ_δ. Also, the estimates of $l^*_N(\psi_\delta)$ have been made with a sector width $\delta = 1°$ to better illustrate the shape of the simulated sample. Using such a small sector width as environmental criteria for design is highly *unconservative* (see, e.g., Forristall (2004) for a discussion on the use of directional environmental criteria).

6.1.2. Estimating design current velocity profiles

Taking advantage of the large sample size (1000 years), a simple and pragmatic way of obtaining N-year design current velocity profiles is to identify a subsample of observations in proximity of a prescribed N-year force level and direction, and then use the corresponding subsample of current velocity profiles directly to construct a design profile. Focusing on critical directional sectors along the 10-year return value line of the resolved forces, $l_N(\psi)$, this approach is used below to obtain estimates of 10-year design current velocity profiles at both Munkskjæra and Salatskjæra. From Fig. 21 and 22 it is noted that, at least for $N > 50$, a longer simulation period would generally be required so that the number of observations at such extreme levels is increased.

At Munkskjæra, we concentrate on the eastward sector $(60°, 100°)$ and the westward sector $(255°, 280°)$. In both sectors, 21 simulated force observations have been identified near the respective peaks of the 10-year return level of $l_N(\psi)$ as indicated by the black crosses in Fig. 21. We thus have a sample of 21 current velocity profiles in each sector, all of which (approximately) give rise to the same total drag force in the same directional sector. To decide the design profiles, we first resolve the current velocity at each depth of each profile into a velocity component in the same direction as the resulting drag force of the profile, the *longitudinal current velocity*, and a component orthogonal to the direction of this force, the *orthogonal current velocity*. The *median* longitudinal current velocity at each depth then serves as a reasonable two-dimensional estimate of the 10-year design current velocity profile in the respective sectors (we preferred the median over the mean as it is less sensitive to outliers). If a three-dimensional profile is desired, the same operation can be performed on the orthogonal current components as well. Even though the resulting, vertically integrated, force due to the orthogonal current profiles is zero, their local effect might be of importance. In Fig. 23, the resulting 10-year design current velocity profiles are shown for both directional sectors together with empirical 10% and 90% quantiles of the velocity components at each depth, obtained from the respective samples of 21 current velocity profiles. As a simple way of validating if the shape of the profiles appears reasonable, the velocity profiles from the measurements causing the 5 largest forces in the two sectors are also included. Though one should be careful not to put too much weight on such a validation, it is reassuring that the shape of the design current profiles is in agreement with the measurements. In sector $(60°, 100°)$, the median longitudinal velocity profile (in the total force direction) in Fig. 23(a) is seen to be relatively uniform with depth. It is somewhat surprising that the lowest velocity of the profile is at the top bin (4 m), however, this is actually supported by the measurements. The orthogonal velocity components in Fig. 23(b) are generally of minor importance, indicating an approximately unidirectional flow. In sector $(255°, 280°)$, the median longitudinal velocity profile in Fig. 23(c) peaks with a velocity of 1 m/s at depth 10 m, decreasing for deeper levels. Again, the orthogonal velocity components in Fig. 23(d) are of minor importance.

At Salatskjæra, the focus is on the main critical sector $(95°, 130°)$. In addition, we investigate sector $(145°, 170°)$ to see if there is any particular difference in the shape of the current profiles south of the local minima at 135°. As for Munkskjæra, 21 current velocity profiles have been identified in each sector in proximity of the 10-year return level of $l_N(\psi)$; see Fig. 22. Following the same procedure of resolving the velocity components at each depth into longitudinal and orthogonal velocity components relative to the total drag force, the resulting 10-year design current profiles for both sectors are shown in Fig. 24. In sector $(95°, 130°)$, the longitudinal design profile in Fig. 24(a) contains its highest velocities at intermediate depths, a shape that is supported by the measurements. A minor anticlockwise rotation is seen for the orthogonal profile in Fig. 24(b). For sector $(145°, 170°)$, the highest velocities of the longitudinal design profile in Fig. 24(c) is found at the deepest levels — a consequence of the high GP shape parameters of the positive major axis components at these depths, cf. Fig. 10(b). This shape is not fully supported by the measurements, however, there seems to be a trend of the lower level velocities increasing more than those at the upper levels, so, as we are extrapolating beyond the measurements, it does not appear unrealistic either. Compared to sector $(95°, 130°)$, both the design profile and the measurements indicate a decrease in the upper level velocities, increasing the relative importance of the lower level velocities.

Overall, the performance of the proposed statistical model and the approach for deriving design current velocity profiles appears to be satisfactory, both at Munkskjæra and Salatskjæra.

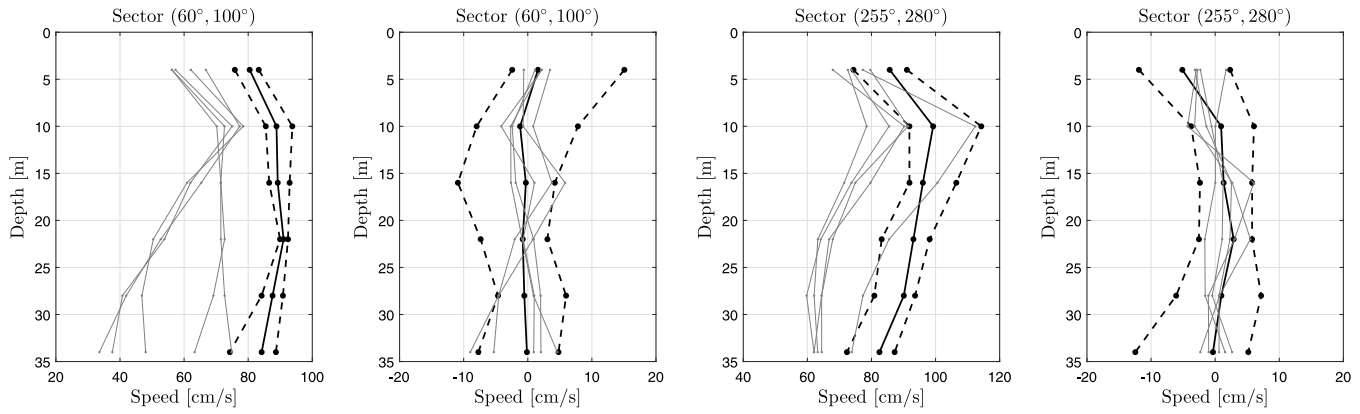

(a) Longitudinal current velocity. (b) Orthogonal current velocity. (c) Longitudinal current velocity. (d) Orthogonal current velocity.

Fig. 23. Munkskjæra; median 10-year design current velocity profiles in the two considered critical directional sectors (solid black) based on the velocity profiles corresponding to the two subsample indicated in Fig. 21. Dashed black lines are 10% and 90% quantiles of the simulated velocity at each depth. Thin grey lines are the velocity profiles from the measurements causing the 5 largest forces in the respective sectors. The longitudinal current velocity is the velocity profile in the direction of the resulting drag force, while the orthogonal current velocity is the velocity profile orthogonal to the resulting drag force.

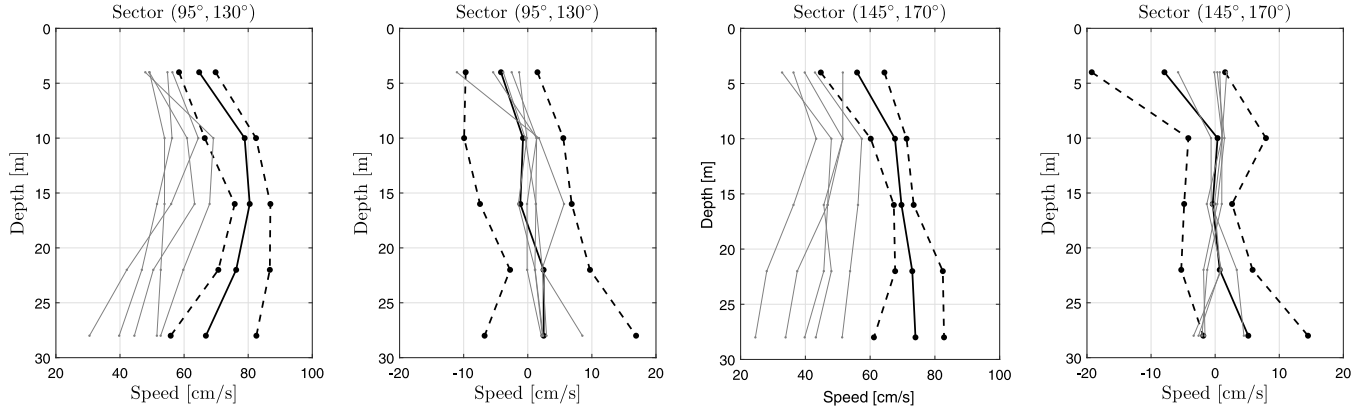

(a) Longitudinal current velocity. (b) Orthogonal current velocity. (c) Longitudinal current velocity. (d) Orthogonal current velocity.

Fig. 24. Salatskjæra; median 10-year design current velocity profiles in the two considered critical directional sectors (solid black) based on the velocity profiles corresponding to the two subsample indicated in Fig. 22. Dashed black lines are 10% and 90% quantiles of the simulated velocity at each depth. Thin grey lines are the velocity profiles from the measurements causing the 5 largest forces in the respective sectors. The longitudinal current velocity is the velocity profile in the direction of the resulting drag force, while the orthogonal current velocity is the velocity profile orthogonal to the resulting drag force.

7. Conclusions and discussion

In this paper we have described a method for statistical modelling of extreme vertical current velocity profiles. The method is based on the conditional extremes model by Heffernan and Tawn (2004), arguably providing the most useful and flexible current approach for modelling extremes in high dimensions.

As illustrated in Fig. 1, we consider current velocity components resolved along major and minor axes at each depth, and decompose the total current into tidal and residual currents using harmonic analysis. A complete marginal model for each of the (both positive and negative) residual current components is then constructed, and the dependence structure is characterized using the conditional extremes model. Estimates for various extremal statistics are acquired by simulating under this model, and extreme total current velocity profiles can be obtained by randomly adding predicted (deterministic) tidal current profiles to realizations of (stochastic) extreme residual current profiles. As implemented, these steps accounts for directionality, spatial and temporal dependence, and non-stationarity introduced by the tide. Based on a long period of simulated current velocity profiles, a simple approach for deriving design current velocity profiles is also proposed.

The statistical method has been tested using ADCP data from two coastal locations in Norway. We have shown that the method provides good extrapolations at both locations. This is confirmed both marginally for each velocity component, jointly for the velocity components at each depth, and for the full velocity profiles — the latter is primarily illustrated in terms of integrated variables (resulting force vector on a circular cylinder due to the current profiles). Compared to the most extreme velocity profiles observed from the measurements, the derived 10-year design current velocity profiles appear realistic, both considering their shape, magnitude, and direction. Even though we have only considered the upper part of the water column, significant change in the velocity as a function of depth is seen for most of the design profiles. The shape of the design profiles is also found to be quite different in the two considered critical directional sectors at both locations. We believe that the proposed method represents a valuable addition to existing methods for deriving extreme current velocity profiles. As the vertical current structure is expected to be more variable in deeper and/or stratified waters, the proposed method will be even more beneficial to apply there.

As presented here, the method makes a number of assumptions which should be commented upon. For instance, the residual current velocities are assumed to be stationary processes. For the data at hand, this is a reasonable assumption, however, at other locations this might not be the case. If there are important seasonal changes, a separate model might be specified for each season (as in Heffernan and Tawn (2004)), with the obvious drawback that each model has less available

Table A.2
Estimated residual current marginal distribution parameters and return levels. The generalized Pareto shape (ξ_i) and scale (σ_i) parameters are estimated by maximum likelihood. The threshold u_{X_i} corresponds to the 95% quantile for the major axis components (M) and the 94% quantile for the minor axis components (m). $x_{i,10y}$ and $x_{i,50y}$ are the estimated 10- and 50-year return levels, respectively, with profile likelihood based 95% confidence intervals in parenthesis. All parameters have been estimated with a minimum peak-to-peak separation time $\tau = 30$ hours. n_{Ci} is the number of observed cluster peak excesses.

Parameter	i	n_{Ci} [–]	u_{X_i} [cm/s]	ξ_i [–]	σ_i [cm/s]	$x_{i,10y}$ [cm/s]	$x_{i,50y}$ [cm/s]	n_{Ci} [–]	u_{X_i} [cm/s]	ξ_i [–]	σ_i [cm/s]	$x_{i,10y}$ [cm/s]	$x_{i,50y}$ [cm/s]
		Munkskjæra						Salatskjæra					
$u^{+}_{RM,1}$	1	74	27.2	−0.36	12.6	58 (55, 70)	60 (57, 76)	67	16.7	−0.08	6.4	48 (40, 80)	54 (44, 113)
$u^{-}_{RM,1}$	2	74	26.2	−0.12	8.4	62 (54, 99)	69 (58, 136)	89	14.4	−0.09	4.8	38 (32, 59)	42 (34, 79)
$u^{+}_{Rm,1}$	3	149	11.7	−0.22	4.5	28 (26, 33)	29 (27, 36)	70	18.0	−0.33	10.6	46 (42, 61)	47 (43, 69)
$u^{-}_{Rm,1}$	4	111	13.7	−0.28	6.3	32 (30, 41)	34 (31, 45)	110	12.4	−0.04	4.7	40 (34, 59)	45 (37, 79)
$u^{+}_{RM,2}$	5	59	31.5	−0.39	16.4	69 (65, 86)	71 (67, 95)	51	18.0	−0.14	8.6	53 (45, 94)	58 (48, 133)
$u^{-}_{RM,2}$	6	67	23.5	−0.03	11.3	85 (68, 165)	100 (74, 267)	77	13.4	0.01	5.2	47 (37, 90)	56 (42, 142)
$u^{+}_{Rm,2}$	7	130	9.9	0.04	3.8	38 (30, 68)	47 (33, 107)	50	18.4	−0.36	13.5	51 (47, 71)	53 (49, 81)
$u^{-}_{Rm,2}$	8	107	11.7	−0.34	8.0	32 (30, 39)	33 (31, 42)	112	10.5	−0.03	4.4	37 (29, 66)	43 (31, 95)
$u^{+}_{RM,3}$	9	57	30.3	−0.39	17.3	70 (66, 87)	72 (69, 97)	51	15.1	−0.01	7.1	56 (42, 151)	66 (46, 290)
$u^{-}_{RM,3}$	10	79	19.9	0.08	7.2	76 (58, 147)	96 (67, 255)	83	11.6	−0.04	4.1	35 (29, 62)	40 (32, 91)
$u^{+}_{Rm,3}$	11	131	8.4	0.11	3.2	39 (28, 74)	50 (33, 126)	51	15.4	−0.27	13.1	54 (48, 85)	57 (51, 106)
$u^{-}_{Rm,3}$	12	126	9.6	−0.09	5.1	34 (29, 51)	39 (31, 67)	113	8.8	−0.05	3.5	29 (24, 46)	33 (26, 63)
$u^{+}_{RM,4}$	13	55	29.2	−0.34	17.4	73 (68, 92)	76 (71, 104)	60	13.4	0.19	4.5	63 (41, 218)	89 (48, 546)
$u^{-}_{RM,4}$	14	80	17.9	0.08	5.9	64 (50, 120)	80 (57, 204)	91	10.6	−0.21	3.9	24 (22, 31)	26 (23, 36)
$u^{+}_{Rm,4}$	15	162	7.6	0.08	2.7	32 (25, 53)	40 (28, 81)	61	13.2	−0.08	8.9	56 (44, 122)	64 (48, 196)
$u^{-}_{Rm,4}$	16	138	8.8	−0.16	5.1	29 (26, 40)	32 (28, 48)	130	7.7	−0.14	2.8	20 (17, 28)	21 (18, 34)
$u^{+}_{RM,5}$	17	55	27.9	−0.34	17.3	71 (66, 93)	74 (69, 106)	64	13.3	0.13	4.8	58 (40, 176)	77 (45, 393)
$u^{-}_{RM,5}$	18	88	17.2	0.08	5.1	57 (44, 110)	71 (50, 187)	93	11.4	−0.16	3.7	26 (23, 38)	28 (24, 46)
$u^{+}_{Rm,5}$	19	189	7.2	−0.10	2.8	21 (19, 27)	24 (20, 33)	71	11.8	−0.01	6.8	53 (40, 115)	63 (44, 191)
$u^{-}_{Rm,5}$	20	142	8.6	−0.19	4.8	27 (24, 34)	29 (26, 39)	128	7.1	−0.20	2.8	18 (16, 23)	19 (16, 27)
$u^{+}_{RM,6}$	21	59	26.6	−0.31	15.5	68 (62, 96)	71 (64, 114)						
$u^{-}_{RM,6}$	22	96	16.8	0.09	4.3	53 (41, 100)	66 (47, 171)						
$u^{+}_{Rm,6}$	23	209	6.9	−0.13	2.8	20 (18, 26)	21 (19, 30)						
$u^{-}_{Rm,6}$	24	156	8.7	−0.11	4.2	29 (25, 39)	32 (27, 47)						

data for inference. Important aspects regarding modelling of extremes of non-stationary sequences can be found in Coles (2001), Chap. 6.

Further, we have assumed that tidal and residual currents are independent. Albeit this appeared reasonable for our data, independence might be a conservative assumption, particularly in shallow water. If tidal–residual current interaction is evident, analogous methods as when estimating extreme sea-levels could probably be applied to account for this (see Tawn (1992), Dixon and Tawn (1999) and Mazas et al. (2014)). Due to the increased dimensionality of the data and the additional dependence modelling, this is however expected to be more challenging to implement for current profiles than for sea-levels.

Inference for marginal and dependence structure has been undertaken (componentwise) using the conventional peaks over threshold method to account for temporal dependence. A major problem for estimation of extreme currents is often to obtain data of adequate length, so using only the cluster peak excesses might seem rather wasteful of data. Fawcett and Walshaw (2007, 2012) argue that more accurate and precise parameter and return level estimates can be obtained by using *all* threshold excesses. This could provide an interesting alternative to the peaks over threshold method used here, and it would also remove the complication of connecting the bulk and tail distribution (cf. Section 5.2.3). It should be noted that temporal dependence still needs to be accounted for when constructing confidence intervals and estimating return levels — this is relatively straightforward in the univariate case, but might prove more defiant for multivariate data such as current profiles. Also, we do not know how this affects the performance of the conditional extremes model.

Another aspect, both relevant for the marginal and the dependence modelling, is the possibility of applying joint estimation instead of componentwise parameter estimation. This is a valuable alternative when there are constraints between the parameters, enabling inferential efficiency to be gained (Heffernan and Tawn, 2004). For instance, one might expect the tail behaviour of a particular velocity component (e.g. positive major axis components) at adjacent depths to display similar tail behaviour. This is equivalent to saying that the generalized Pareto parameters of the velocity component varies relatively smoothly with depth. Similarly, the dependence parameters for a given velocity component are also expected to vary relatively smoothly with depth. Treating depth as a covariate, parameter smoothness could for instance be controlled within a penalized likelihood framework (see, e.g., Chavez-Demoulin and Davison (2005), Jonathan et al. (2014)). In this respect, ideas from the piecewise stationary extreme value model of Ross et al. (2018) seems particularly interesting to use together with the modelling strategy proposed herein (though, clearly adding complexity to the analysis).

Threshold selection is an important step in the proposed method, both when fitting the marginal tail model and the dependence model. Due to the large number of considered residual current components, a suitable common threshold corresponding to a given non-exceedance probability was selected in the present work; one for the major axis components and one for the minor axis components. Common threshold selection (or other automated procedures) is inevitable due to the large number of possible threshold choices. Still, as also commented by Jonathan et al. (2012), a more satisfactory procedure than the one presented here would generally be desirable. Estimating models for different threshold levels, and then averaging over the models to incorporate uncertainty in threshold selection, is a possible (but comprehensive) solution; see, e.g., Northrop et al. (2016) or Ross et al. (2017).

In the conditional simulation (cf. Section 5.4), there is one assumption which should be mentioned in particular. Subsequent to having simulated a value of the conditioning variate Y_i, it concerns how to determine which components of the remaining profile $\mathbf{Y}_{-i}$ that should be observed and which should not. We have assumed that it is appropriate to determine this by drawing an arbitrary $\hat{\mathbf{z}}_{|i}$ and let the $(d/2-1)$ observed components of $\hat{\mathbf{z}}_{|i}$ control which components of $\mathbf{Y}_{-i}$ that are observed. As commented in Section 5.4, a simplification involved here is that the probability of observing a particular $Y_{j|i}$

does not depend on the magnitude of the simulated Y_i (the number of observed $Y_{j|i}$ in the conditional simulation thus follows a binomial distribution). It is therefore important that the conditional threshold is set sufficiently high in the dependence modelling. For the data at hand, this assumption did not affect the results in any critical way. However, we expect that the robustness of the method could be improved by also modelling this type of dependence — this is probably easier to accommodate if the current direction is explicitly considered as a covariate in the statistical model.

Acknowledgements

We would like to thank three anonymous reviewers for thorough and thoughtful comments. This work was supported by the Research Council of Norway through the Centres of Excellence funding scheme, project number 223254 – NTNU AMOS, and through the Centres for Research-Based Innovation funding scheme, project number 237790 – EXPOSED.

Appendix A. Residual current marginal distribution parameters and return levels

Estimated residual current marginal distribution parameters and return levels are given in Table A.2.

References

Balkema, A.A., de Haan, L., 1974. Residual life time at great age. Ann. Probab. 2 (5), 792–804, URL http://www.jstor.org/stable/2959306.
Barnett, V., 1976. The ordering of multivariate data. J. R. Stat. Soc. Ser. A General 139 (3), 318.
Beirlant, J., Goegebeur, Y., Segers, J., Teugels, J., 2004. Statistics of Extremes: Theory and Applications. John Wiley & Sons.
Bitner-Gregersen, E.M., Bhattacharya, S.K., Chatjigeorgiou, I.K., Eames, I., Ellermann, K., Ewans, K., Hermanski, G., Johnson, M.C., Ma, N., Maisondieu, C., Nilva, A., Rychlik, I., Waseda, T., 2014. Recent developments of ocean environmental description with focus on uncertainties. Ocean Eng. 86, 26–46.
Boon, J.D., 2004. Secrets of the Tide: Tide and Tidal Current Analysis and Predictions, Storm Surges and Sea Level Trends. Woodhead Publishing.
Broch, O.J., Daae, R.L., Ellingsen, I.H., Nepstad, R., Bendiksen, E.Å., Reed, J.L., Senneset, G., 2017. Spatiotemporal dispersal and deposition of fish farm wastes: A model study from central norway. Front. Mar. Sci. 4.
Bruserud, K., Haver, S., 2017. Uncertainties in current measurements in the northern north sea. J. Atmos. Ocean. Technol. 34 (4), 855–876.
Caires, S., Sterl, A., 2005. 100-year return value estimates for ocean wind speed and significant wave height from the ERA-40 data. J. Clim. 18 (7), 1032–1048.
Chavez-Demoulin, V., Davison, A.C., 2005. Generalized additive modelling of sample extremes. J. R. Stat. Soc. Ser. C. Appl. Stat. 54 (1), 207–222.
Chavez-Demoulin, V., Davison, A.C., 2012. Modelling time series extremes. REVSTAT 10 (1), 109–133.
Choulakian, V., Stephens, M.A., 2001. Goodness-of-fit tests for the generalized pareto distribution. Technometrics 43 (4), 478–484, URL http://www.jstor.org/stable/1270819.
Codiga, D.L., 2011. Unified Tidal Analysis and Prediction: Using the UTide Matlab Functions. Tech. Rep., Graduate School of Oceanography, University of Rhode Island.
Coles, S., 2001. An Introduction to Statistical Modeling of Extreme Values. Springer.
Coles, S.G., Dixon, M.J., 1999. Likelihood-based inference for extreme value models. Extremes 2 (1), 5–23.
Coles, S., Heffernan, J., Tawn, J., 1999. Dependence measures for extreme value analyses. Extremes 2 (4), 339–365.
Coles, S.G., Tawn, J.A., 1991. Modelling extreme multivariate events. J. R. Stat. Soc. Ser. B Stat. Methodol. 53 (2), 377–392, URL http://www.jstor.org/stable/2345748.
Coles, S.G., Tawn, J.A., 1994. Statistical methods for multivariate extremes: An application to structural design. J. R. Stat. Soc. Ser. C Appl. Stat. 43 (1), 1.
Davison, A.C., Padoan, S.A., Ribatet, M., 2012. Statistical modeling of spatial extremes. Statist. Sci. 27 (2), 161–186.
Davison, A.C., Smith, R.L., 1990. Models for exceedances over high thresholds. J. R. Stat. Soc. Ser. B Stat. Methodol. 52 (3), 393–442, URL http://www.jstor.org/stable/2345667.
de Zea Bermudez, P., Kotz, S., 2010a. Parameter estimation of the generalized Pareto distribution—Part I. J. Statist. Plann. Inference 140 (6), 1353–1373.
de Zea Bermudez, P., Kotz, S., 2010b. Parameter estimation of the generalized Pareto distribution—Part II. J. Statist. Plann. Inference 140 (6), 1374–1388.
Dixon, M.J., Tawn, J.A., 1999. The effect of non-stationarity on extreme sea-level estimation. J. R. Stat. Soc. Ser. C. Appl. Stat. 48 (2), 135–151.
DNV, 2014. DNV-RP-C205, Environmental conditions and environmental loads. Det Norske Veritas.
Doodson, A.T., 1921. The harmonic development of the tide-generating potential. Proc. R. Soc. Lond. Ser A Math. Phys. Eng. Sci. 100 (704), 305–329.
Drees, H., Janßen, A., 2017. Conditional extreme value models: fallacies and pitfalls. Extremes 20 (4), 777–805.
Eastoe, E., Koukoulas, S., Jonathan, P., 2013. Statistical measures of extremal dependence illustrated using measured sea surface elevations from a neighbourhood of coastal locations. Ocean Eng. 62, 68–77.
Eastoe, E.F., Tawn, J.A., 2012. Modelling the distribution of the cluster maxima of exceedances of subasymptotic thresholds. Biometrika 99 (1), 43–55.
Fawcett, L., Walshaw, D., 2007. Improved estimation for temporally clustered extremes. Environmetrics 18 (2), 173–188.
Fawcett, L., Walshaw, D., 2012. Estimating return levels from serially dependent extremes. Environmetrics 23 (3), 272–283.
Flinchem, E.P., Jay, D.A., 2000. An introduction to wavelet transform tidal analysis methods. Estuar. Coast. Shelf Sci. 51 (2), 177–200.
Foreman, M.G.G., 1977. Manual for Tidal Heights Analysis and Prediction. Tech. Rep., Institute of Ocean Sciences, Patricia Bay.
Foreman, M.G.G., 2004. Manual for Tidal Currents Analysis and Prediction. Tech. Rep., Institute of Ocean Sciences, Patricia Bay.
Foreman, M.G.G., Cherniawsky, J.Y., Ballantyne, V.A., 2009. Versatile harmonic tidal analysis: Improvements and applications. J. Atmos. Ocean. Technol. 26 (4), 806–817.
Foreman, M.G.G., Henry, R.F., 1989. The harmonic analysis of tidal model time series. Adv. Water Resour. 12 (3), 109–120.
Forristall, G.Z., 2004. On the use of directional wave criteria. J. Waterw. Port Coast. Ocean Eng. 130 (5), 272–275.
Forristall, G.Z., Cooper, C.K., 1997. Design current profiles using empirical orthogonal function (EOF) and inverse FORM methods. In: Offshore Technology Conference.
Godin, G., 1972. The Analysis of Tides. University of Toronto Press.
Grimshaw, S.D., 1993. Computing maximum likelihood estimates for the generalized pareto distribution. Technometrics 35 (2), 185–191.
Heffernan, J.E., Resnick, S.I., 2007. Limit laws for random vectors with an extreme component. Ann. Appl. Probab. 17 (2), 537–571.
Heffernan, J.E., Tawn, J.A., 2004. A conditional approach for multivariate extreme values (with discussion). J. R. Stat. Soc. Ser. B Stat. Methodol. 66 (3), 497–546.
Horsburgh, K.J., Wilson, C., 2007. Tide-surge interaction and its role in the distribution of surge residuals in the North Sea. J. Geophys. Res. 112 (C8).
Huang, C.-C., Tang, H.-J., Liu, J.-Y., 2008. Effects of waves and currents on gravity-type cages in the open sea. Aquacult. Eng. 38 (2), 105–116.
ISO, 2015. ISO 19901-1, Petroleum and Natural Gas Industries — Specific Requirements for Offshore Structures — Part 1: Metocean Design and Operating Considerations. European Committee for Standardization.
Jolliffe, I.T., 2002. Principal Component Analysis. Springer.
Jonathan, P., Ewans, K., Flynn, J., 2012. Joint modelling of vertical profiles of large ocean currents. Ocean Eng. 42, 195–204.
Jonathan, P., Ewans, K., Randell, D., 2013. Joint modelling of extreme ocean environments incorporating covariate effects. Coast. Eng. 79, 22–31.
Jonathan, P., Ewans, K., Randell, D., 2014. Non-stationary conditional extremes of northern North Sea storm characteristics. Environmetrics 25 (3), 172–188.
Jonathan, P., Flynn, J., Ewans, K., 2010. Joint modelling of wave spectral parameters for extreme sea states. Ocean Eng. 37 (11–12), 1070–1080.
Keef, C., Papastathopoulos, I., Tawn, J.A., 2013. Estimation of the conditional distribution of a multivariate variable given that one of its components is large: Additional constraints for the Heffernan and Tawn model. J. Multivariate Anal. 115, 396–404.
Keef, C., Tawn, J., Svensson, C., 2009. Spatial risk assessment for extreme river flows. J. R. Stat. Soc. Ser. C. Appl. Stat. 58 (5), 601–618.
Kristiansen, D., Aksnes, V., Su, B., Lader, P., Bjelland, H.V., 2017. Environmental description in the design of fish farms at exposed locations. In: 36th International Conference on Ocean, Offshore and Arctic Engineering, vol. 6. ASME.
Leadbetter, M.R., 1983. Extremes and local dependence in stationary sequences. Z. Wahrscheinlichkeitstheor. Verwandte Geb. 65 (2), 291–306.
Leadbetter, M.R., 1991. On a basis for 'peaks over threshold' modeling. Statist. Probab. Lett. 12 (4), 357–362.
Leadbetter, M.R., Lindgren, G., Rootzen, H., 1983. Extremes and Related Properties of Random Sequences and Processes. Springer.
Lohrmann, A., 1998. Comparison of Buoy Mounted NDP Current Velocity Data with Upward Loking ADCP Data. Tech. Rep., Nortek AS.
Longuet-Higgins, M.S., 1953. Mass transport in water waves. Philos. Trans. R. Soc. Lond. Ser. A Math. Phys. Sci. 245 (903), 535–581, URL http://www.jstor.org/stable/91480.
Lu, Y., Lueck, R.G., 1999. Using a broadband ADCP in a tidal channel. Part I: Mean flow and shear. J. Atmos. Ocean. Technol. 16 (11), 1556–1567.
Mackay, E.B.L., Challenor, P.G., Bahaj, A.S., 2011. A comparison of estimators for the generalised pareto distribution. Ocean Eng. 38 (11–12), 1338–1346.
Mayer, D.A., Virmani, J.I., Weisberg, R.H., 2007. Velocity comparisons from upward and downward acoustic doppler current profilers on the west florida shelf. J. Atmos. Ocean. Technol. 24 (11), 1950–1960.

Mazas, F., Kergadallan, X., Garat, P., Hamm, L., 2014. Applying POT methods to the revised joint probability method for determining extreme sea levels. Coast. Eng. 91, 140–150.

Munk, W., Hasselmann, K., 1964. Super-resolution of tides. Stud. Oceanogr. 339–344.

Nortek, 2017. The Comprehensive Manual. Nortek AS.

Northrop, P.J., Attalides, N., Jonathan, P., 2016. Cross-validatory extreme value threshold selection and uncertainty with application to ocean storm severity. J. R. Stat. Soc. Ser. C. Appl. Stat. 66 (1), 93–120.

Nystrom, E.A., Rehmann, C.R., Oberg, K.A., 2007. Evaluation of mean velocity and turbulence measurements with ADCPs. J. Hydraul. Eng. 133 (12), 1310–1318.

Pickands, J., 1975. Statistical inference using extreme order statistics. Ann. Statist. 3 (1), 119–131, URL http://www.jstor.org/stable/2958083.

Prandle, D., Wolf, J., 1978. The interaction of surge and tide in the North Sea and River Thames. Geophys. J. Int. 55 (1), 203–216.

Pugh, D.T., 1982. Estimating extreme currents by combining tidal and surge probabilities. Ocean Eng. 9 (4), 361–372.

Pugh, D.T., Vassie, J.M., 1976. Tide and surge propagation off-shore in the Dowsing region of the North Sea. Dtsch. Hydrogr. Z. 29 (5), 163–213.

Pugh, D.T., Vassie, J.M., 1978. Extreme sea levels from tide and surge probability. In: Proceedings of 16th Conference on Coastal Engineering. ASCE, pp. 911–930.

Pugh, D.T., Vassie, J.M., 1980. Applications of the joint probability method for extreme sea level computations. In: Proceedings of the Institution of Civil Engineers. Proc. Inst. Civ. Eng. 69 (4), 959–975.

Pugh, D., Woodworth, P., 2014. Sea-Level Science: Understanding Tides, Surges, Tsunamis and Mean Sea-Level Changes. Cambridge University Press.

Raghupathi, L., Randell, D., Ewans, K., Jonathan, P., 2016. Non-stationary estimation of joint design criteria with a multivariate conditional extremes approach. In: 35th International Conference on Ocean, Offshore and Arctic Engineering, vol. 3. ASME.

Robinson, M.E., Tawn, J.A., 1997. Statistics for extreme sea currents. J. R. Stat. Soc. Ser. C. Appl. Stat. 46 (2), 183–205.

Röhrs, J., Christensen, K.H., Hole, L.R., Broström, G., Drivdal, M., Sundby, S., 2012. Observation-based evaluation of surface wave effects on currents and trajectory forecasts. Ocean Dyn. 62 (10–12), 1519–1533.

Ross, E., Randell, D., Ewans, K., Feld, G., Jonathan, P., 2017. Efficient estimation of return value distributions from non-stationary marginal extreme value models using Bayesian inference. Ocean Eng. 142, 315–328.

Ross, E., Sam, S., Randell, D., Feld, G., Jonathan, P., 2018. Estimating surge in extreme North Sea storms. Ocean Eng. 154, 430–444.

Sætre, R., 2007. The Norwegian Coastal Current: Oceanography and Climate. Fagbokforlaget.

Scarrott, C., MacDonald, A., 2012. A review of extreme value threshold estimation and uncertainty quantification. REVSTAT 10 (1), 33–60.

Seim, H.E., Edwards, C.R., 2007. Comparison of buoy-mounted and bottom-moored ADCP performance at gray's reef. J. Atmos. Ocean. Technol. 24 (2), 270–284.

Silverman, B.W., 1986. Density Estimation for Statistics and Data Analysis. Springer US.

Smith, R.L., Weissman, I., 1994. Estimating the extremal index. J. R. Stat. Soc. Ser. B Stat. Methodol. 56 (3), 515–528, URL http://www.jstor.org/stable/2346124.

Tawn, J.A., 1988. An extreme-value theory model for dependent observations. J. Hydrol. 101 (1–4), 227–250.

Tawn, J., 1990. Discussion on Models for exceedances over high thresholds (by A. C. Davison and R. L. Smith). J. R. Stat. Soc. Ser. B Stat. Methodol. 52 (3), 428–429.

Tawn, J.A., 1992. Estimating probabilities of extreme sea-levels. J. R. Stat. Soc. Ser. C Appl. Stat. 41 (1), 77–93.

Tawn, J.A., Vassie, J.M., 1989. Extreme sea levels: the joint probabilities method revisited and revised. Proc. Inst. Civ. Eng. 87 (3), 429–442.

Tromans, P.S., Vanderschuren, L., 1995. Response based design conditions in the North Sea: Application of a new method. In: Offshore Technology Conference.

Winant, C., Mettlach, T., Larson, S., 1994. Comparison of buoy-mounted 75-kHz acoustic doppler current profilers with vector-measuring current meters. J. Atmos. Ocean. Technol. 11 (5), 1317–1333.

Winterstein, S.R., Haver, S., Jha, A.K., Kvingedal, B., Nygaard, E., 2011. Turkstra profiles of North Sea currents: Wider than you'd think. In: 30th International Conference on Ocean, Offshore and Arctic Engineering, vol. 2. ASME.

Wunsch, C., 2015. Modern Observational Physical Oceanography. Princeton University Press.